# A three-dimensional dynamical model of current sheet formation in a coronal loop

D. W. Longcope

*Department of Physics, Montana State University, Bozeman, MT 59717*

dana@solar.physics.montana.edu

and

A. A. Van Ballegooijen

*Harvard-Smithsonian Center for Astrophysics, 60 Garden Street, Cambridge, MA 02138*

## ABSTRACT

We develop a three-dimensional model for the time evolution of a slender coronal loop anchored in multiple isolated photospheric flux elements. As a result of the composite photospheric boundaries, the coronal field comprises multiple flux domains. The model shows that motion at the footpoints results in current singularities developing along separators between domains. Motion at one end of the loop creates a non-singular Alfvénic pulse. Repeated reflections from the complex photospheric boundaries change the pulse's current into a surface singularity traveling along the separator ribbon. Final relaxation leads to an equilibrium which is current-free within all of the coronal domains and contains a separator current sheet. The relation of the equilibrium current to the footpoint displacements confirms previous quasi-static models of three-dimensional separator current sheets.

*Subject headings:* Sun: magnetic fields — Sun: corona — MHD

## 1. Introduction

Models of the solar corona have often appealed to the hypothesis that its magnetic field develops current sheets when the photospheric footpoints move (Sweet 1958; Parker 1957).

Most famously Parker put forth the theory of topological dissipation (Parker 1972) whereby the coronal field develops tangential discontinuities (current sheets) which heat the corona. Van Ballegooijen (1985) modeled this process in a long, thin flux tube whose photospheric ends were smoothly sheared. He concluded that the thickness of coronal current layers decreased steadily without reaching zero, and so there would be no current sheet. Numerical simulations appear consistent with this conclusion, although it is debatable that they would be capable of identifying a genuine singularity were it to occur (Mikic *et al.* 1989; Longcope and Sudan 1994; Hendrix and van Hoven 1996). Analytical treatments have not, however, reached a consensus concerning those conditions under which current singularities are permissible (Antiochos 1987; Van Ballegooijen 1988; Parker 1994; Longcope and Strauss 1994a).

In the model originally proposed by Parker, and adopted by subsequent investigators, coronal magnetic field is anchored to the photosphere uniformly ($B_z$ = constant at $z = 0$), and a smooth flow velocity is prescribed everywhere on that plane. The prescribed flow condition reflects the dramatic difference in typical plasma $\beta$ between corona and photosphere. The controversy over current-sheet development pertains only to models such as this with smoothly anchored field subject to smooth prescribed flows.

One potentially significant observation, neglected by this model, is that actual coronal loops are anchored in the photosphere to discrete, kilogauss flux tubes surrounded by much weaker fields. Each flux tube fans out with height, and neighboring flux tubes merge to form a more uniform field higher up in the corona. The flux tubes are subject to convective flows associated with the solar granulation, which push the flux tubes into the intergranular lanes (Berger and Title 1996). At the photosphere the flux tubes have strong magnetic field, $B$ = 1500 – 1700 G at the height where the continuum optical depth $\tau_{5000} = 1$ in the field-free medium, corresponding to plasma $\beta$ = 0.09 - 0.4 inside (Zayer *et al.* 1990; Frutiger and Solanki 2001). Apparently, these relatively strong fields do not prevent the flux tubes from being pushed into the intergranular lanes.

A coronal magnetic field anchored in discrete photospheric elements is likely to differ, in several key respects, from one anchored uniformly and subject to smooth prescribed flows. Field lines map from concentrated elements to the more uniform coronal field in a complex and discontinuous manner. If the flow velocity in the photosphere were smooth, even between the insides and outsides of flux tubes, it would generate a coronal flow which is far less smooth (Van Ballegooijen *et al.* 1998). Nor is it *a priori* clear that the flow field within a magnetic flux tube, where $\beta \sim 0.3$ will bear any relation to that outside. The external flow consists of the convective motions which move the flux tubes to intergranular lanes, while the internal motions are more likely to be a response to magnetic forces in the flux tube.

It is possible that small scale structure, such as current sheets, might result from coronal dynamics subject to discrete photospheric anchoring. Indeed, Longcope (2001) proposed a model for magnetic equilibria anchored in discrete photospheric sources. The discrete anchoring allows coronal field lines to be grouped into *domains* according to the positive and negative sources to which they are anchored. Minimizing the magnetic energy of the coronal field, subject to constraints on the flux in each domain, leads to current sheets along certain domain interfaces. Features called *separators*, which lie at the interface of four domains, will in general contain current sheets in this model. Since it permits footpoint motions internal to photospheric sources, the flux constraint is less restrictive than the line-tying constraint imposed by Parker.

This model of *flux-constrained equilibria* offers insight into the location of coronal fine-structure arising due to discrete anchoring. Furthermore, the minimization procedure quantifies the energy attributable to the footpoint mapping, and therefore available upon reconnection. Being an equilibrium model, however, it sheds no light on the process by which a continuous magnetic field develops current sheets. Nor has it been possible to solve the Euler-Lagrange equations resulting from the minimization, except in two-dimensional cases.

The present work will explore some of the effects discrete anchoring might have on coronal dynamics. It will proceed by proposing a model for a long, thin coronal loop anchored to several distinct photospheric sources. We propose a "boundary condition" on the coronal dynamics which accounts for the complex mapping to the photospheric elements and the distinct internal and external flows there. When the photosphere at one end of the loop initiates a disturbance, the opposing boundary condition reflects the disturbance with a current/vorticity sheet. After repeated reflection the coronal field approaches a state in which a wave carries singular current localized entirely to the field's *separator ribbon*. If the wave is allowed to dissipate while keeping the photospheric velocities bounded, the field approaches a singular equilibrium. An example of such an equilibrium, exhibited analytically, satisfies the Euler-Lagrange equation of the flux-constrained model.

The next section presents the general dynamical model for the corona as well as a chromospheric field which maps it to the discrete photospheric sources. The dynamics of the corona are described by the equations of reduced MHD (Strauss 1976). Boundary conditions on the coronal dynamics are applied at the *merging height*, which is the interface between corona and chromosphere. Section 3 applies this general model to a specific configuration of photospheric sources, undergoing a smooth deformation. This shows the progressive development of a current sheet through repeated reflection of coronal Alfvén waves. In Section 4 we add a mechanism for wave dissipation, and show that this leads to a singular equilibrium. Section 5 discusses the significance of this model for coronal magnetic fields.

## 2. The Model

To facilitate analysis we assume a large aspect ratio geometry, similar to that of Van Ballegooijen (1985). We take the domain to be a long, thin cylinder, bounded by perfect conductors, and with a total length $L + 2h$, much greater than its radius, $a$. The cylinder's axis runs from $z = -h$ to $z = L + h$, with a central region $0 < z < L$ representing the corona and two end regions representing chromospheric layers, as shown in fig. 1. (The terms "corona" and "chromosphere" are used here as short-hand for magnetic geometries; their temperatures will not be part of this model.)

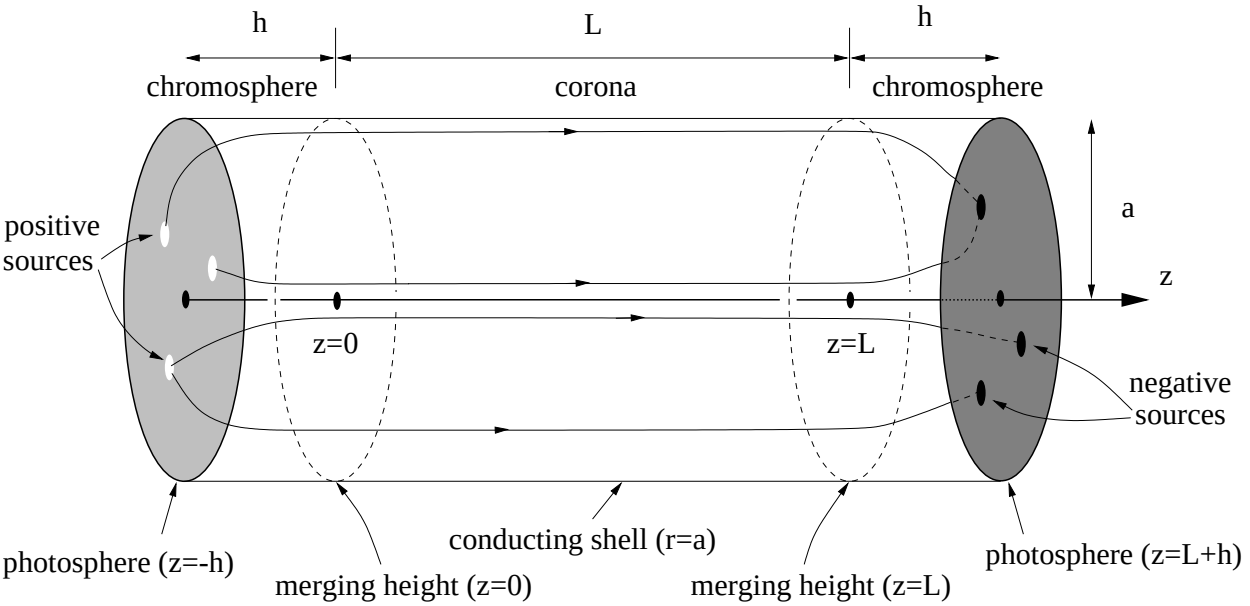


Fig. 1.— The geometry of the model. The cylinder's radius $a$ has been exaggerated for clarity. The model assumes $a \ll h \ll L$. The axial coronal loop is anchored in multiple discrete photospheric sources (black and which circles). Sample field lines from each of the domains are shown.

The end boundaries of the cylinder are conducting photospheres on which are distributed discrete, isolated flux sources. These sources represent the small ($\sim 10^{17}$–$10^{18}$ Mx), magnetic elements observed to compose the photospheric field (Zwaan 1987). They can be modeled either as point sources or extended regions separated from one another by field-free photosphere. A prescribed "external" photospheric flow field will dictate the motion of the sources within the plane. Flows inside a source region, however, will respond to the internal dynamics of a magnetic flux tube and are thus not prescribed like the external flow.

The magnetic field in the chromospheric layers expands from localized photospheric sources to a relatively uniform field in the corona. The planes at $z = 0$ and $z = L$, called *merging heights*, will be the formal boundaries between these two magnetic regimes. We will assume that the cylinder is sufficiently narrow that $h \gg a$, assuring that the axial field is uniform in the corona. The only role of the chromospheric field is to map the field from photospheric flux elements to the corona, i.e. from $z = -h$ to $z = 0$ and from $z = L + h$ to $z = L$.

The two photospheric surfaces, representing opposite polarity regions, contain sources of opposite sign. $N_+$ positive photospheric sources with fluxes $\Phi_i^+$, are located at positions $\mathbf{r}_i^+$, on the $z = -h$ plane (the positive photosphere). Similarly, $N_-$ negative sources with fluxes $\Phi_j^-$, are located at $\mathbf{r}_j^-$ on the $z = L + h$ plane. To be consistent with a divergence-free magnetic field, each photosphere must contain the same total flux,

$$\Phi_0 \equiv \sum_i \Phi_i^+ = -\sum_j \Phi_j^- \quad . \tag{1}$$

The mean axial field strength in the corona, $\bar{B}_z = \Phi_0/\pi a^2$, is set by the photospheric flux. In this geometry almost every field line begins a positive source at $z = -h$ and ends at a negative source at $z = L + h$, and $B_z > 0$ everywhere inside the cylinder.

The chromosphere is assumed thick enough, $h \gg a$, that the axial magnetic field will be uniform at its top ($z = 0$ or $z = L$). The dynamics of the corona may therefore be treated using the equations of reduced MHD (Strauss 1976). Motion of the photospheric sources will map to motions at the merging height, which will be considered boundary motion for the reduced MHD corona.

### 2.1. The chromospheric region

In our model, the chromosphere serves as a means of mapping the coronal field down to the discrete photospheric sources. Since we are exploring coronal dynamics, which have a relatively long time scale, we expect the chromosphere to remain in equilibrium. A potential

magnetic field, $\mathbf{B} \simeq -\nabla\chi$, provides the simplest equilibrium capable of matching an arbitrary distribution of sources. The current incident from the corona can be neglected over distances $\sim h$ so an assumption that the chromosphere is force-free implies it is approximately potential. Within a 1500 G source, $\beta \sim 0.3$, in the photosphere and decreases rapidly with height above the photosphere. Thus the magnetic chromosphere may be approximated as force-free, however, non-magnetic portions obviously cannot. Non-magnetic regions do not, however, map to the corona, so it is not clear how they might affect our model. For expediency we will adopt a potential chromosphere and return later to examine how different the field-line mapping might be under more realistic conditions.

The scalar potential $\chi$ must satisfy Laplace's equation with a homogeneous Neumann boundary condition at $r = a$. The general solution in each chromosphere is

$$\chi(r,\phi,z) \;=\; -\,\bar{B}_z\, z \;\pm\; \sum_{mn} C^{(\pm)}_{m,n}\, J_m(j'_{m,n} r/a)\, e^{im\phi}\, e^{-|z-z^\pm| j'_{m,n}/a} \quad , \tag{2}$$

where $J_m$ is the Bessel function of order $m$ and $j'_{m,n}$ is the $n^{\rm th}$ zero of its derivative. The axial magnetic field at photospheric plane $z = z^\pm$ is given by the sources. Point sources at $\mathbf{r}^\pm_{j,\perp}$ provide the condition

$$\begin{aligned} B_z(r,\phi,z=z^\pm) \;&=\; \bar{B}_z \;+\; a^{-1} \sum_{mn} C^{(\pm)}_{m,n} j'_{m,n}\, J_m(j'_{m,n} r/a)\, e^{im\phi} \\ &=\; \sum_j \Phi^\pm_j\, \delta(\mathbf{r}_\perp - \mathbf{r}^\pm_{j,\perp}) \quad , \end{aligned} \tag{3}$$

where $\mathbf{r}_\perp$ is $(r,\phi)$. This expression may be inverted to give the explicit coefficients

$$C^\pm_{m,n} \;=\; \frac{a j'_{m,n}}{\pi(j'^2_{m,n} - m^2) J^2_m(j'_{m,n})} \sum_j \Phi^\pm_j\, J_m(j'_{m,n} r^\pm_j/a)\, e^{-im\phi^\pm_j} \quad . \tag{4}$$

The coefficients $C^\pm_{m,n}$ may also be found for photospheric sources of finite extent, rather than points.

The potential (2) approaches its coronal form, $\chi = -\bar{B}_z z$, exponentially as $|z - z^\pm|$ increases (see fig. 2). We assume that by the merging height, $|z - z^\pm| = h$, the field has become approximately uniform $B_z \simeq \bar{B}_z$.

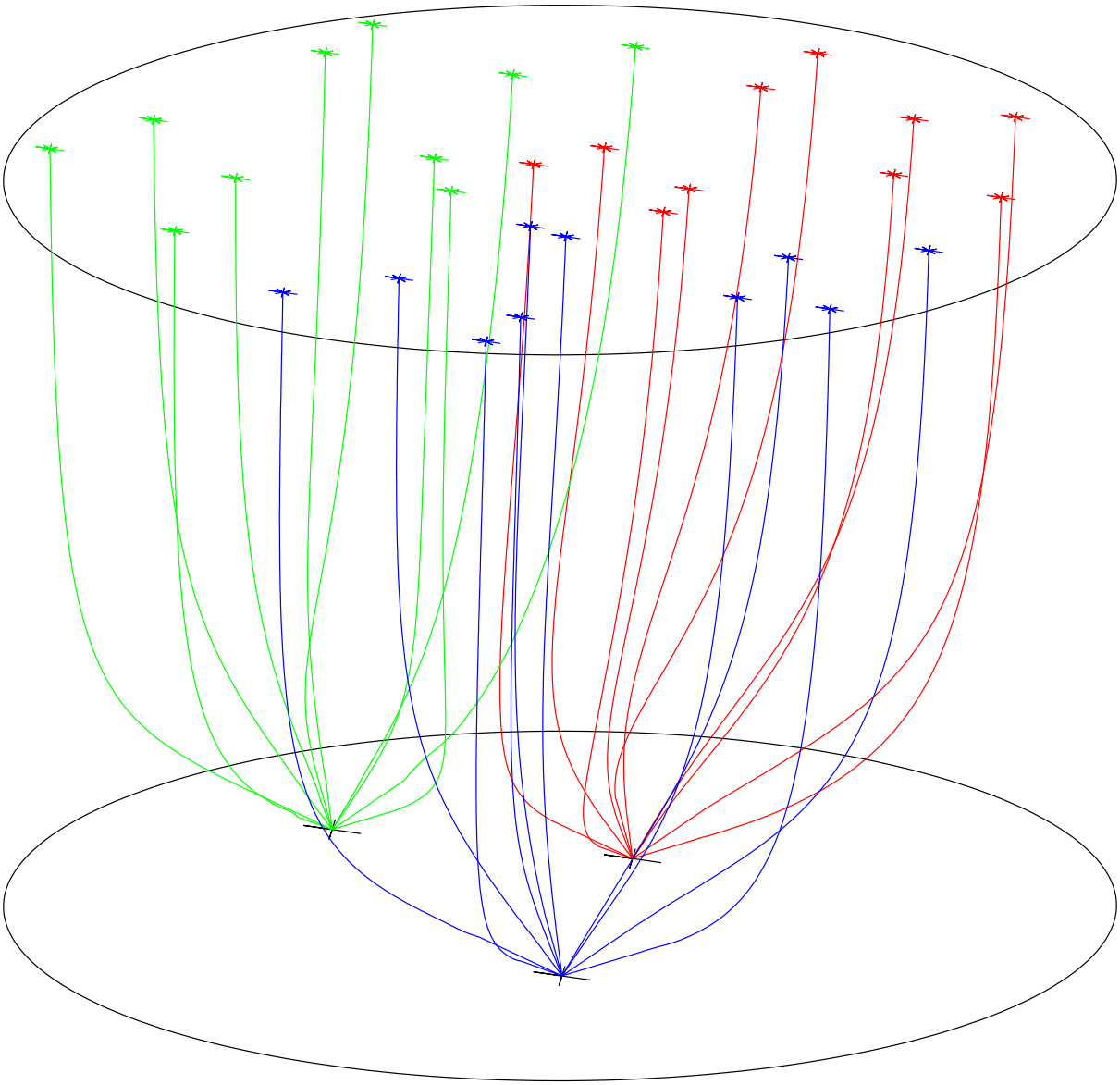

Fig. 2.— The chromospheric field lines from the sources. The field becomes uniform by the merging height $z = 0$.

Chromospheric field lines may be traced from their sources to the merging height as shown in fig. 2. This mapping partitions the positive (negative) merging layer into $N_+$ ($N_-$) non-overlapping regions $\mathcal{S}_i^{\pm}$, as shown in figs. 3a and 3b. All of the flux $|\Phi_i^{\pm}|$ originating in source $i$ maps to this region, so its area is

$$|\mathcal{S}_i^{\pm}| \;=\; \frac{|\Phi_i^{\pm}|}{\bar{B}_z} \quad . \tag{5}$$

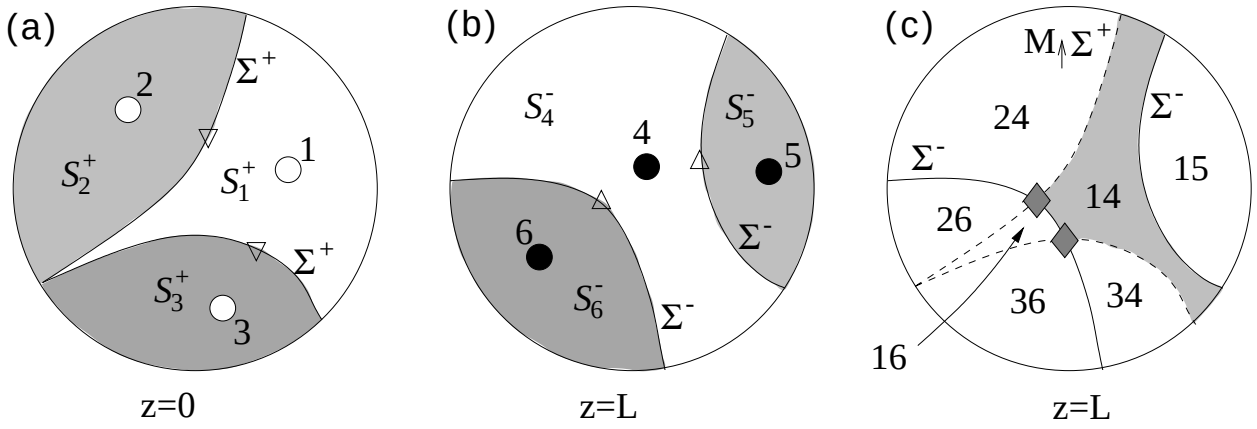


Fig. 3.— An example of regions $\mathcal{S}_i^{\pm}$ and their mappings between merging heights. (a) Three positives sources (open circles) and two positive nulls ($\nabla$) at $z = -h$ give rise to two separatrix curves $\Sigma^+$ (solid) and three regions (different shadings) at the merging height $z = 0$. (b) The same plot for the $z = L$ merging height. The nulls at $z = L + h$ are of the negative type ($\triangle$). (c) The positive regions $\mathcal{S}_i^+$ mapped to $z = L$ form 7 domains, labeled $ij$ (domain $\mathcal{D}_{14}$ is shaded). The image $\mathcal{M}_{\uparrow}\Sigma^+$ are shown dashed. The two separators are shown as grey diamonds.

The boundaries between regions occur where separatrices intersect the merging layer. We will call these curves of intersection $\Sigma^+$ and $\Sigma^-$ respectively. At the positive merging height ($z = 0$) these separatrices will be the fan surfaces of positive (B-type) null points within the chromosphere ($-h \leq z < 0$), hereafter called a *positive separatrix*. All of the nulls will be confined to the photospheric planes, since each all of the sources there are the same sign.

## 2.2. The corona

### *2.2.1. Field lines*

The axial component of the coronal field will be taken to be perfectly uniform $B_z(\mathbf{r}) = \bar{B}_z$. The field will not be purely axial, since motions at the photospheric boundaries can introduce a perpendicular component $\mathbf{B}_\perp \sim \epsilon \bar{B}_z$, where $\epsilon \equiv a/L \ll 1$. The complete magnetic field may be written in terms of a re-scaled flux function $A(\mathbf{r}_\perp, z)$

$$\mathbf{B}(\mathbf{r}_\perp, z) \;=\; \bar{B}_z \,(\,\hat{\mathbf{z}} \;+\; \nabla A \times \hat{\mathbf{z}}\,) \quad . \tag{6}$$

The ordering assumed above, often called the reduced MHD ordering, requires that $|\nabla_\perp A| \sim \epsilon$.

A coronal field line can be written as a curve $\mathbf{r}_\perp(z)$ parameterized by axial coordinate $z$; it satisfies the equation

$$\frac{d\mathbf{r}_\perp}{dz} \;=\; \nabla_\perp A \times \hat{\mathbf{z}} \quad . \tag{7}$$

Coronal field lines induce an area preserving mapping between the positive and negative merging heights. The mapping $\mathcal{M}_\uparrow$ takes a point $\mathbf{r}^0_\perp$ on the positive merging height ($z = 0$) to point $\mathbf{r}^L_\perp$ at the negative merging height($z = L$):

$$\mathbf{r}^L_\perp \;=\; \mathcal{M}_\uparrow \, \mathbf{r}^0_\perp \quad . \tag{8}$$

The inverse mapping will be denoted $\mathcal{M}_\downarrow$. These mappings depend implicitly on the flux function $A(\mathbf{r}_\perp, z, t)$ through equation (7).

Mapping the positive regions $\mathcal{S}^+_i$ to the negative merging height exhibits all of the flux domains, as in fig. 3c. The intersection of region $\mathcal{S}^-_j$ with the image of $\mathcal{S}^+_i$ is the domain $\mathcal{D}_{ij}$. The area of this intersection gives the total flux in the domain

$$\psi_{ij} \;=\; \bar{B}_z \,\left|\, \left(\mathcal{M}_\uparrow \, \mathcal{S}^+_i\right) \cap \mathcal{S}^-_j \,\right| \quad . \tag{9}$$

The same domain appears at the opposite merging layer with the same flux.

A separator is the intersection of positive and negative separatrices. In a generic potential magnetic field, pairs of surfaces intersect along curves called *separator field lines*. Separators cross the negative merging height at $\Sigma^- \cap \mathcal{M}_\uparrow \Sigma^+$, (diamonds in fig. 3c), and cross the positive merging height at $\Sigma^+ \cap \mathcal{M}_\downarrow \Sigma^-$.

### *2.2.2. Dynamics*

We will assume the corona to have a constant mass density $\rho_0$ and a very small plasma $\beta$. The plasma velocity will then be incompressible and principally perpendicular to $\hat{\mathbf{z}}$. This can be written in terms of a rescaled stream function $\varphi(\mathbf{r}_\perp, z)$

$$\mathbf{v} \;=\; \nabla\varphi \times \hat{\mathbf{z}} \quad . \tag{10}$$

Under the reduced MHD ordering, $|\nabla\varphi| \sim \epsilon v_{\rm A}$ where $v_{\rm A} = \bar{B}_z/\sqrt{4\pi\rho_0}$ is the axial Alfvén speed.

Using definitions (6) and (10) in the vorticity equation and induction equation yields a coupled system known as reduced MHD (Strauss 1976). These may be concisely written in terms of the Poisson bracket

$$[\; f,\; g\;] \equiv \frac{\partial f}{\partial y}\frac{\partial g}{\partial x} - \frac{\partial f}{\partial x}\frac{\partial g}{\partial y} = (\nabla_\perp f \times \hat{\mathbf{z}}) \cdot \nabla_\perp g \quad , \tag{11}$$

which is anti-symmetric in its arguments. The ideal reduced MHD equations are

$$\frac{\partial \Omega}{\partial t} \;+\; [\;\varphi,\; \Omega\;] \;=\; v_{\rm A}^2 \left( \frac{\partial J}{\partial z} \;+\; [\;A,\; J\;] \right) \tag{12}$$

$$\frac{\partial A}{\partial t} \;+\; [\;\varphi,\; A\;] \;=\; \frac{\partial \varphi}{\partial z} \quad , \tag{13}$$

where the rescaled vorticity and current are defined

$$\Omega(\mathbf{r}_\perp, z) \;=\; -\nabla_\perp^2 \varphi \quad , \tag{14}$$

$$J(\mathbf{r}_\perp, z) \;=\; -\nabla_\perp^2 A \quad . \tag{15}$$

These are nonlinear equations for the functions $\varphi(\mathbf{r}_\perp, z, t)$ and $A(\mathbf{r}_\perp, z, t)$.

The reduced MHD equations admit solutions which are Alfvén wave packets propagating purely rightward ($W_+$) or leftward ($W_-$)

$$A(\mathbf{r}_\perp, z, t) \;=\; W_\pm(\mathbf{r}_\perp,\; v_{\rm A} t \mp z) \quad , \tag{16}$$

$$\varphi(\mathbf{r}_\perp, z, t) \;=\; \mp v_{\rm A}\, W_\pm(\mathbf{r}_\perp,\; v_{\rm A} t \mp z) \quad . \tag{17}$$

Since arbitrary functions $W_\pm(\mathbf{r}_\perp,\zeta)$ are nonlinear solutions of (12) and (13) even large amplitude wave packets propagate at the constant axial Alfvén speed without dispersion. In a superposition of leftward and rightward waves the nonlinear term will cause some change in each.

Initial conditions for eqs. (12) and (13) consist of complete specification of magnetic field and velocity through $A(\mathbf{r}_\perp,z,t=0)$ and $\varphi(\mathbf{r}_\perp,z,t=0)$. In order to determine $\varphi(\mathbf{r}_\perp,z)$ from the elliptic equation (14), conditions must be supplied on all perpendicular boundaries. Since the cylinder walls are rigid and perfectly conducting the flow and magnetic fields must be tangent to them. A sufficient perpendicular boundary condition is

$$\varphi(r=a,\phi,z,t) \;=\; 0 \quad , \quad A(r=a,\phi,z,t) \;=\; 0 \quad . \tag{18}$$

The energy of the system is the sum of its kinetic and magnetic contributions

$$E \;=\; \int \left\{ \tfrac{1}{2}\rho_0 \left|\nabla_\perp\varphi\right|^2 \;+\; \frac{\bar{B}_z^2}{8\pi}|\nabla_\perp A|^2 \right\} d\mathbf{r} \quad , \tag{19}$$

excluding the large energy of the axial field. (This unchanging contribution to the energy is larger by $\sim\epsilon^{-2}$). Equations (12) and (13) along with boundary conditions (18) gives the energy change

$$\frac{dE}{dt} \;=\; \frac{\bar{B}_z^2}{8\pi}\int\limits_{z=L} \nabla_\perp\varphi\cdot\nabla_\perp A\, d\mathbf{r}_\perp \;-\; \frac{\bar{B}_z^2}{8\pi}\int\limits_{z=0} \nabla_\perp\varphi\cdot\nabla_\perp A\, d\mathbf{r}_\perp \quad , \tag{20}$$

which result from Poynting flux through the merging heights.

Finally, since the system is hyperbolic in the $z,t$ coordinates it is necessary to specify the inward waves at each boundary,

$$A(\mathbf{r}_\perp,z=0,t) - v_{\scriptscriptstyle A}^{-1}\varphi(\mathbf{r}_\perp,z=0,t) \;=\; 2U^+(\mathbf{r}_\perp,t) \quad , \tag{21a}$$

$$A(\mathbf{r}_\perp,z=L,t) + v_{\scriptscriptstyle A}^{-1}\varphi(\mathbf{r}_\perp,z=L,t) \;=\; 2U^-(\mathbf{r}_\perp,t) \quad . \tag{21b}$$

The functions $U^\pm$ may be specified explicitly or in terms of independent linear combinations of $A$ and $\varphi$ at that boundary.

Two versions of (21) common in the literature are rigid and open (non-reflecting) endplanes. The non-reflecting boundary condition is achieved by specifying no inward waves $U^\pm=0$. Equation (20) shows that such a boundary condition leads to energy decrease. Rigid ends, on the other hand, are stationary and thus have vanishing stream-function, $\varphi=0$. This can be achieved in eq. (21) through the condition $U(\mathbf{r}_\perp,t)=\frac{1}{2}A(\mathbf{r}_\perp,t)$. This will convert an inward wave to an equal outward wave and cause the Poynting flux to vanish.

### 2.3. The Merging Height

Photospheric motions are mapped to motions at the merging heights, $z = 0$ and $z = L$, through the chromospheric field. We will consider separately flows in the unmagnetized photosphere (external motions) and flows with a magnetic source (internal motions). Prescribed external flows, if present, move each source as a whole thereby changing the entire chromospheric field. This change is manifest at the merging height as an evolution in the regions $\mathcal{S}_i^{\pm}$ and as motions of their boundaries $\Sigma^{\pm}$. Internal photospheric motions do not change the chromospheric field, rather they translate chromospheric field lines as a whole, maintaining their potential configuration. This maps to a motion at the merging height which is internal to the region $\mathcal{S}_i^{\pm}$.

Internal photospheric motion can originate from below the photosphere, as an evolution of the flux tube. When this upward-propagating disturbance is mapped to the merging height it can translate to extremely large coronal velocities (Van Ballegooijen *et al.* 1998). It is also possible for magnetic forces from the corona to drive internal flows which then propagate downward along the sub-photospheric flux tube as a generalized torsional wave (Longcope and Welsch 2000). These two possibilities are manifest at the merging height as a specified inward wave-form and a transmitted outward wave-form respectively (inward and outward are here used relative to the corona). A stationary photosphere maps to a stationary merging height which would perfectly reflect all outward waves into inward waves.

In this work we are concerned with coronal dynamics so we will disregard the possibility of prescribed inward waves. We will further assume that outward propagating torsional waves cross the photosphere with no reflection. This means that *any inward propagating wave will be current-free within each region* $\mathcal{S}_i^{\pm}$. The boundary functions $U^{\pm}$ must therefore be harmonic inside the regions $\mathcal{S}_i^{\pm}$

$$\begin{aligned} \nabla_\perp^2 U^+ &= 0 \quad , \quad \mathbf{r}_\perp \notin \Sigma^+ \\ \nabla_\perp^2 U^- &= 0 \quad , \quad \mathbf{r}_\perp \notin \Sigma^- \quad . \end{aligned}$$

Setting to zero the Laplacians of the boundary conditions (21) within the region interiors gives

$$\nabla_\perp^2 \varphi^0(\mathbf{r}_\perp, t) = -v_{\scriptscriptstyle A}\, J(\mathbf{r}_\perp, z{=}0, t) \quad , \quad \mathbf{r}_\perp \notin \Sigma^+ \tag{22a}$$

$$\nabla_\perp^2 \varphi^L(\mathbf{r}_\perp, t) = v_{\scriptscriptstyle A}\, J(\mathbf{r}_\perp, z{=}L, t) \quad , \quad \mathbf{r}_\perp \notin \Sigma^- \tag{22b}$$

where $\varphi^0(\mathbf{r}_\perp, t)$ and $\varphi^L(\mathbf{r}_\perp, t)$ are the stream functions at each merging height. This condition is applied everywhere but on the separatrix curves of that merging height, so it applies only to the region interiors.

According to this boundary condition a torsional Alfvén wave propagating into the chromosphere is "absorbed" by the photospheric source; in fact its propagation continues along the flux tube. We adopt this absorbing boundary condition as an expedient means of studying the approach to coronal equilibrium and the development of coronal current sheets. A more physical boundary condition would permit some reflection from the chromosphere, due to its smaller Alfvén speed. This will not change the basic results of our analysis, and we return to discuss its effect in the final section.

Equation (22) must be solved for the velocity stream functions $\varphi^{0,L}(\mathbf{r}_\perp, t)$ to provide useful boundary conditions for (13). By assumption, boundary flows are confined to source regions $\mathcal{S}_j^\pm$, so the separatrix curves $\Sigma^\pm$ must be streamlines. If the separatrix curves form a single interconnected web joining the walls $r = a$, then this can be satisfied by the condition

$$\varphi^0(\mathbf{r}_\perp, t) \;=\; 0 \quad , \quad \mathbf{r}_\perp \;\in\; \Sigma^+ \quad , \tag{23a}$$

$$\varphi^L(\mathbf{r}_\perp, t) \;=\; 0 \quad , \quad \mathbf{r}_\perp \;\in\; \Sigma^- \quad . \tag{23b}$$

If there are several unconnected pieces to the separatrix web, then a different constant value of $\varphi$ will appear on each piece.

Equations (22) and (23) are at the heart of our model for coronal evolution. They encapsulate the dynamics of the photosphere and chromosphere to provide a boundary condition on the coronal dynamics. Hereafter we consider the coronal dynamics alone using (22) and (23) as boundary conditions. We will refer to the merging heights as boundaries.

One motivation for our choice of boundary conditions is that they always lead toward the state of minimum coronal energy. Using eqs. (22) and (23) in energy equation (20), gives an energy change

$$\frac{dE}{dt} \;=\; -\frac{\bar{B}_z^2}{8\pi v_{\scriptscriptstyle A}} \int |\nabla_\perp \varphi^L|^2 \, d\mathbf{r}_\perp \;-\; \frac{\bar{B}_z^2}{8\pi v_{\scriptscriptstyle A}} \int |\nabla_\perp \varphi^0|^2 \, d\mathbf{r}_\perp \quad , \tag{24}$$

which is a decrease whenever there is boundary motion. The boundary flows are area preserving, so the various flux domains $\psi_{ij}$ are automatically preserved. This implies that the coronal will automatically approach a flux-constrained equilibrium (Longcope 2001).

Implementing the combined conditions requires the solution of a two-dimensional Poisson's equation, (22), within each region $\mathcal{S}_j^\pm$ subject to homogeneous Dirichlet boundary conditions (23). The solutions, $\varphi^{0,L}$, will thus have continuous derivatives within the regions, and be continuous across the region boundaries $\Sigma^\pm$. The solution will, however, have discontinuous normal derivatives across the boundaries. These discontinuities are a natural manifestation of mapping discontinuities at the separatrices. While the flow is discontinuous at the region boundaries, it does not diverge there as it might under prescribed internal flows at the photosphere (Van Ballegooijen *et al.* 1998).

## 3. An example

To demonstrate the model above we apply it to a simple case with two positive and two negative sources. The positive sources have equal fluxes $\Phi_1 = \Phi_2 = \Phi_0/2$, and are placed symmetrically about the $z$ axis: $r_1 = r_2 = d_+$, $\phi_1 = -\phi_2 = \pi/2$ (see fig. 4a). The negative sources also have equal fluxes $\Phi_3 = \Phi_4 = -\Phi_0/2$ and are symmetric about the $z$ axis, but at an angle $\theta$ relative to the positive sources: $r_3 = r_4 = d_-$, $\phi_3 = -\phi_4 = \pi/2 + \theta$. This angle is initially $\theta_0$, and the corona is in a static potential state: $A(\mathbf{r}_\perp, z, 0) = \varphi(\mathbf{r}_\perp, z, 0) = 0$. The negative boundary is then rotated by an angle $\Delta\theta$ creating a disturbance in the corona. In this section we calculate the dynamic response of the corona to movements of the photospheric sources.

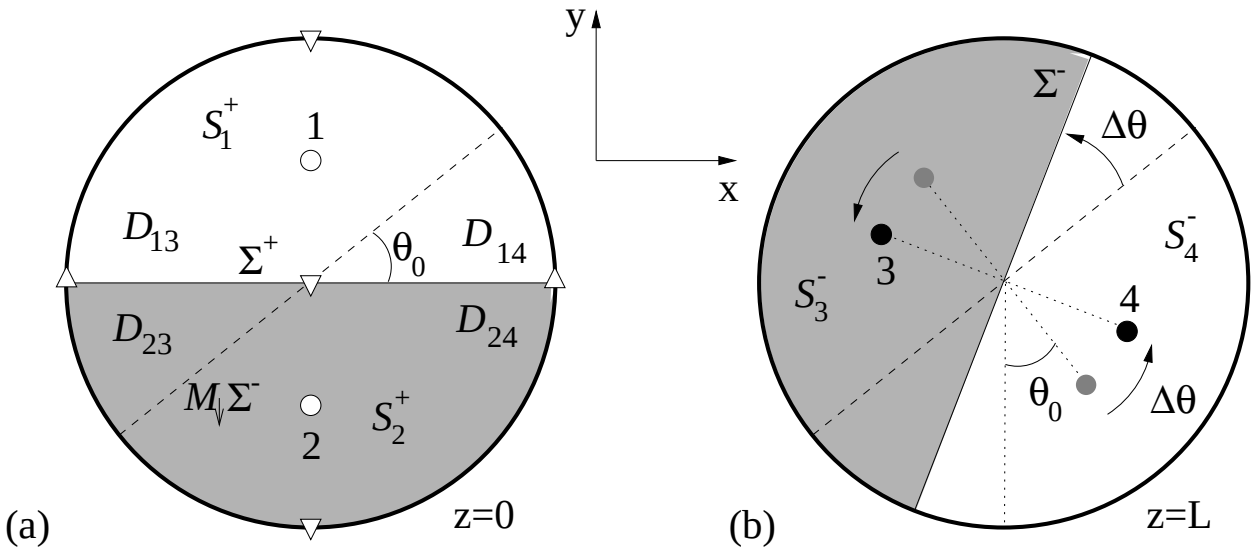


Fig. 4.— Photospheric sources in the example. (a) The two positive photospheric sources (white circles) and five null points (triangles). The positive separatrix $\Sigma^+$ (solid line) is the fan-surface of the central null and divides the circle into regions $\mathcal{S}_1^+$ and $\mathcal{S}_2^+$ (shaded). The image of the negative separatrix $\mathcal{M}_\downarrow\Sigma^-$, at $t < 0$ (dashed line) further subdivides the region into four domains $\mathcal{D}_{ij}$ (labeled). (b) The same plot at the negative photosphere. The grey circles show the locations of sources 3 and 4 at $t < 0$, the black circles show their locations after a rotation $\Delta\theta$. The dashed and solid lines are $\Sigma^-$ before and after the rotation.

The chromospheric magnetic field is not trivial, even for this very simple distribution of sources. Nevertheless, it can be shown on the basis of symmetry that the magnetic field vanishes at five points in each photospheric plane. The positive photosphere, $z = -h$, contains a positive null ($\nabla$) at $(x, y) = 0$ two more positive nulls at $(x, y) = (\pm a, 0)$ and two negative nulls ($\triangle$) at $(x, y) = (0, \pm a)$, as shown in fig. 4. The fan surface of the central positive null, hereafter called the *positive separatrix*, is the $x$–$z$ plane, crossing the merging height along the line $y = 0$, this is $\Sigma^+$. The fan surface of each each negative null is the photospheric plane itself, $z = -h$, and the fan surfaces of the outer positive nulls are the cylindrical boundary $r = a$. The negative photosphere, $z = L + h$, is similar except that the fan surface of the central null (a negative null) crosses the merging height, $z = L$, at an angle $\theta$; this is $\Sigma^-$.

In the initial state all coronal field lines are straight and the mapping $\mathcal{M}$ is the identity transformation. The four domains are therefore wedges, $\mathcal{D}_{14}$, $\mathcal{D}_{13}$, $\mathcal{D}_{23}$ and $\mathcal{D}_{24}$, counter-clockwise from the $\phi = 0$. The area of each wedge gives the fractional flux in its domain. Thus

$$\psi_{14} = \psi_{23} = \frac{\theta_0}{2\pi}\Phi_0 \quad , \quad \psi_{13} = \psi_{24} = \frac{\pi - \theta_0}{2\pi}\Phi_0 \quad . \tag{25}$$

(It is possible to take $\theta_0 \leq \pi/2$ without loss of generality by labeling the sources so that $\psi_{13} \geq \psi_{14}$.)

A necessary condition for current sheet formation, according the theory of flux constrained equilibria, is that a graph of the domains contain at least one circuit (Longcope 2001). Four domains are the minimum needed for a circuit, so provided $\theta_0 \neq 0$, this example contains the necessary complexity to obtain a current sheet.

A separator runs along the $z$ axis connecting the two central nulls. The field strength on the separator field line is $B = 0$ at the null, increasing rapidly to $B = \bar{B}_z$ by the merging height, constant through the coronal and falling back to $B = 0$ at the other photosphere. This field line passes through any closed path formed from field lines in the domain graph's circuit (Longcope 2001). It is this property which makes it the site of an equilibrium current sheet, according to the theory of flux-constrained equilibria.

The locations of the nulls and their fan surfaces do not depend on the source separations $d_+$ and $d_-$. External flow in the form of photospheric convergence or divergence, changing only the separation but not the angles, will change the chromospheric field but not the separatrix locations. In our model coronal dynamics are driven entirely by changes in the separatrices at the merging heights $\Sigma^\pm$. Thus our model predicts no coronal evolution resulting from a pure convergence or divergence of photospheric sources.

A simple external motion which generates a coronal response is a pure rotation of one

photospheric plane. We consider a rotation of the negative photosphere by an angle $\Delta\theta$ over a time $\tau_{\rm m}$,

$$\theta(t) \;=\; \theta_0 \;+\; \Delta\theta \int_0^t P(t'/\tau_{\rm m})\, dt'/\tau_{\rm m} \quad , \tag{26}$$

where $P(t)$ is a square pulse of unit length and unit magnitude. (The foregoing results would be unchanged if $P$ were replaced by a smoother pulse shape.) The rotation angle $\Delta\theta$ can be either positive or negative, but for concreteness we will consider $\Delta\theta > 0$. In the analysis that follows we assume that $\tau_{\rm m} < \tau_{\rm A}$ so the pulse fits within the corona.

### 3.1. The initial pulse

The photospheric rotation will launch a leftward propagating Alfvén wave. Taking the boundary motion to be a rigid rotation $\varphi^L \sim -\dot\theta r^2/2$, persisting for a time $\tau_{\rm m}$ gives a leftward propagating pulse of axial length $\ell_{\rm m} = v_{\rm A}\tau_{\rm m}$

$$W_-(r,\phi,\zeta) \;=\; \frac{\Delta\theta}{2\ell_{\rm m}}\,(a^2 - r^2)\,P[(\zeta - L)/\ell_{\rm m}] \quad . \tag{27}$$

The current distribution is uniform within the pulse

$$J(r,\phi,z,t) \;=\; -\,\nabla_\perp^2 W_- \;=\; \frac{2\Delta\theta}{\ell_{\rm m}}\,P[t/\tau_{\rm m} - (L-z)/\ell_{\rm m}] \quad , \tag{28}$$

carrying a total current $I_0 = 2(\Delta\theta/\ell_{\rm m})\Phi_0$.

Once the boundary rotation has ceased the energy in the system will have risen from zero to

$$E_0 \;=\; \frac{1}{8\pi^2}\,\frac{\Phi_0^2\Delta\theta^2}{\ell_{\rm m}} \quad . \tag{29}$$

This energy has been imparted to the system by the boundary motion through a Poynting flux.

### 3.2. The first reflection

At time $t = \tau_{\rm A} = L/v_{\rm A}$ the initial leftward pulse strikes the positive merging height $z = 0$, creating a rightward reflection. The form of the incident pulse permits an exact solution of its reflection. During the reflection $A = W_+ + W_-$ and $\varphi = v_{\rm A}(W_- - W_+)$, which may depend on general combinations of $z$ and $t$. Using these in both (12) and (13) shows

that the incident pulse $W_-$ is unchanged by the interaction, and the reflection must satisfy the single equation

$$\left(\frac{\partial}{\partial z} \; + \; v_{\rm A}^{-1}\frac{\partial}{\partial t}\right) W_+ \; + \; 2\frac{\Delta\theta}{\ell_{\rm m}}\, P[(v_{\rm A}t + z - L)/\ell_{\rm m}]\, \frac{\partial W_+}{\partial \phi} \;=\; 0 \quad . \tag{30}$$

The final term is the interaction of the reflection with the incident pulse, given by (27). As a result the reflected pulse undergoes a rotation

$$W_+(r,\phi,z,t) \;=\; U[r,\phi-\phi_0(z,t)]\, P[(v_{\rm A}t - z - L)/\ell_{\rm m}] \quad , \tag{31}$$

where $U(r,\phi)$ describes its profile at the merging height (where $\phi_0 = 0$). Equation (30) indicates that the reflection travels along the helical field lines. The rotation angle

$$\phi_0(z,t) \;=\; \frac{2\Delta\theta}{\ell_{\rm m}} \int_0^z P[(2z' + v_{\rm A}t - z - L)/\ell_{\rm m}]\, dz' \quad , \tag{32}$$

is a general function of $z$ and $t$ until $t > \tau_{\rm A} + \tau_{\rm m}$ when it becomes a purely rightward wave, depending only on $\zeta = v_{\rm A}t - z$.

The incident pulse creates a flow $\varphi^0(\mathbf{x}_\perp, t)$ on the positive merging height. The stream function must satisfy (22a)

$$\nabla_\perp^2 \varphi^0 \;=\; -\, v_{\rm A}\, J(\mathbf{r}_\perp, 0, t) \;=\; -\,\frac{2\Delta\theta}{\tau_{\rm m}} \quad , \quad y \neq 0 \tag{33}$$

where the final expression uses the fact that the current is that of the incident pulse alone. Equation (33) must be solved with $\varphi^0 = 0$ along $y = 0$, the separatrix surface $\Sigma^+$. During the interval $\tau_{\rm A} < t < \tau_{\rm A} + \tau_{\rm m}$ the solution is

$$\varphi^0(r,\phi,t) \;=\; \frac{\Delta\theta a^2}{\tau_{\rm m}} \left[\frac{a^2 - r^2}{2a^2} \; - \; H\left(\frac{r}{a},\phi\right)\right] \tag{34}$$

where $H$ is a continuous harmonic function, chosen to make $\varphi^0 = 0$ at $y = 0$ and $r = a$. The harmonic function can be written in terms of a complex function of a complex coordinate variable, $H(r,\phi) = \mathrm{Re}\{\hat{H}(re^{i\phi})\}$. The complex function,

$$\hat{H}(w) \;=\; \tfrac{1}{2}(1-w^2) \; + \; \frac{i}{\pi}(2 - w^{-2} - w^2)\ln\left(\sqrt{\frac{1+w}{1-w}}\right) + \; \frac{i}{\pi}(w^{-1} + w) \quad , \tag{35}$$

derived in an Appendix, is analytic in the upper half plane ($y > 0$). The function $H(r,\phi)$ in the lower half plane is the reflection of that in the upper half plane. The resulting stream function, shown in fig. 5a, consists of eddies localized to source regions $\mathcal{S}_1^+$ and $\mathcal{S}_2^+$.

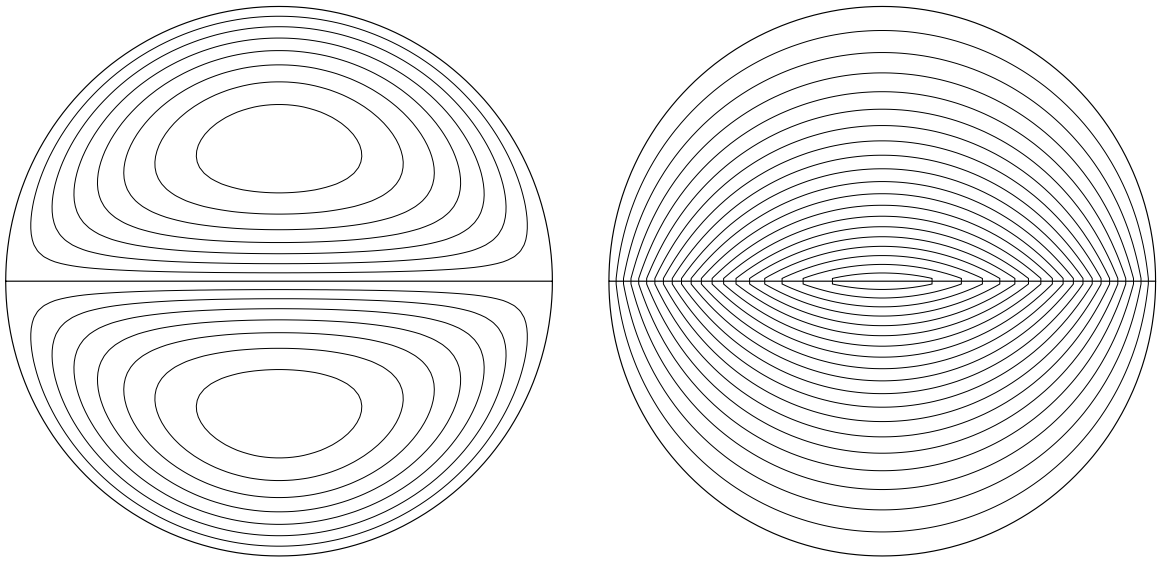

Fig. 5.— The result of the impact of the initial pulse on the positive merging height. (a) The stream function $\varphi^0(x, y)$, shows the counter-clockwise internal motions of each region. The boundary condition $\varphi^0 = 0$ are applied at each of the dark curves. (b) The profile of the rightward propagating wave $W_+(x, y)$. The dark line shows the current sheet.

Across the $x$ axis, the stream function is continuous, but its normal derivative is not. This results in a discontinuous velocity

$$v_x(x,0\pm) \;=\; \left.\frac{\partial\varphi^0}{\partial y}\right|_{y=\pm 0} \;=\; \pm\,\frac{\Delta\theta a}{\tau_{\rm m}}\,K(x/a) \quad , \tag{36}$$

where the vorticity sheet density is characterized by the function

$$K(x) \;=\; {\rm Im}\left\{\hat{H}'(x)\right\} \;=\; -\,\frac{2}{\pi x^3}\left[(x^4-1)\ln\left(\sqrt{\frac{1+x}{1-x}}\right)+x-x^3\right] \quad , \tag{37}$$

also derived in the Appendix.

The profile of the rightward wave is found from the stream-function and the leftward wave

$$W_+(r,\phi) \;=\; W_-(r,\phi) \;-\; v_{\rm A}^{-1}\,\varphi^0(r,\phi) \;=\; \frac{a^2\Delta\theta}{\ell_{\rm m}}\,H(r/a,\phi) \quad , \quad z=0 \quad . \tag{38}$$

The current in the rightward wave is confined to the separatrix $\Sigma^+$, as a surface current

$$J \;=\; -\,\nabla_\perp^2 W_+ \;=\; \frac{2a\Delta\theta}{\ell_{\rm m}}\,K(x/a)\,\delta(y) \quad , \tag{39}$$

whose total current $I_1 = 0.8106(\Delta\theta/\ell_{\rm m})\Phi_0$ is derived in the appendix.

Replacing the profile $H(r/a,\phi)$ in expression (31) gives the complete axial structure of the rightward pulse during and after its interaction with the incident leftward pulse

$$W_+(r,\phi,z,t) \;=\; \frac{a^2\Delta\theta}{\ell_{\rm m}}\,H[r/a,\,\phi-\phi_0(z,t)]\,P[(v_{\rm A}t-z-L)/\ell_{\rm m}] \quad . \tag{40}$$

A current sheet arising from a singularity in $\nabla_\perp^2 H$, follows the surface $\phi=\phi_0(z)$, given by expression (32). At the pulse's trailing edge, the sheet is aligned with the positive separatrix $\Sigma^+$, at $\phi_0=0$. Once it is clear of the incident pulse the leading edge, $v_{\rm A}t-z=L$, is tilted to $\phi_0=\Delta\theta$. This orientation matches the same separatrix surface at the negative merging height, $\mathcal{M}_\uparrow\Sigma_+$ (see fig. 6).

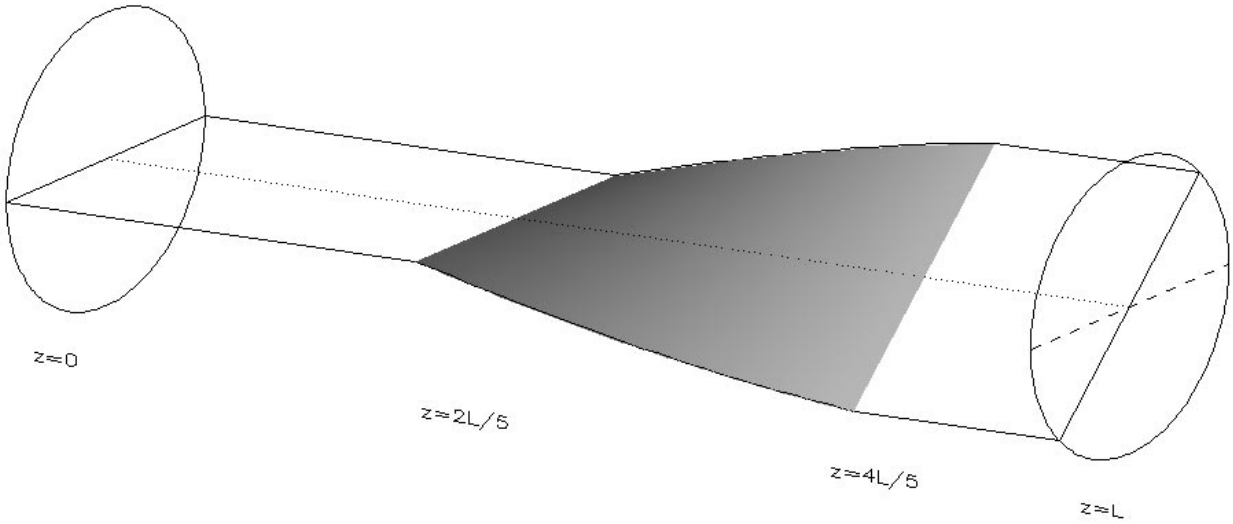


Fig. 6.— The first reflection of pulse with $\tau_{\rm m} = 2\tau_{\rm A}/5$, and $\Delta\theta = \pi/4$ at time $t = 1.8\tau_{\rm A}$. The solid line traces the outer edges of the positive separatrix from $z = 0$ (at $\phi = 0$) to $z = L$ (at $\phi = \Delta\theta = \pi/4$). The dashed line shows its orientation prior to movement ($t < 0$). The shaded surface is the location of the axial current sheet.

Note that the axial current $J$ is confined to the length of the pulse by the shape-function $P(\zeta)$ in eq. (40). The current closes radially along the leading and trailing edges where $\partial A/\partial z \sim P'(\zeta)$.

Between the leading and trailing edges the current sheet has the helical pitch

$$q \;\equiv\; \frac{\partial\phi_0}{\partial z} \;=\; \frac{\Delta\theta}{\ell_{\rm m}}\,\{\; P[(v_{\rm A}t+z-L)/\ell_{\rm m}] \;+\; P[(v_{\rm A}t-z-L)/\ell_{\rm m}]\;\} \quad , \tag{41}$$

which is right handed ($q > 0$). Outside the region of interaction the helical pitch is $q = \Delta\theta/\ell_{\rm m}$, and twice as great within it.

At the completion of the first reflection the total energy in the system has decreased to

$$E_1 \;=\; \frac{\bar{B}_z^2\ell_{\rm m}}{4\pi}\int |\nabla_\perp W_+|^2\,d\mathbf{r}_\perp \;=\; \frac{0.6211}{8\pi^2}\,\frac{\Phi_0^2\Delta\theta^2}{\ell_{\rm m}} \quad . \tag{42}$$

This is 62% of the energy in the initial pulse reflecting the extent to which the motion of the footpoints of sources 1 and 2 were able to lower the energy. As in any Alfvén wave this is equal parts magnetic and kinetic energy.

### 3.3. The second reflection

At $t = 2\tau_{\rm A}$ the rightward wave strikes the stationary negative boundary at $z = L$. At this point it is a current/vorticity sheet confined to the positive separatrix. The response of the merging height depends on the location of the negative separatrix $\Sigma^-$ relative to this sheet. In the special case where $\theta_0 = 0$ they coincide, $\mathcal{M}_\uparrow\Sigma^+ = \Sigma^-$. We consider this special case before the more general situation $\theta_0 \neq 0$.

#### *3.3.1. The special case $\theta_0 = 0$*

When it reaches the negative merging height the current in the rightward wave is confined to the positive separatrix. For the special case $\theta_0 = 0$ this is also the negative separatrix $\Sigma^-$ so

$$\nabla_\perp^2\varphi^L \;=\; J \;=\; 0 \quad , \quad \mathbf{r}_\perp \notin \Sigma^- \quad . \tag{43}$$

The homogeneous boundary condition (23) admits only the trivial solution $\varphi^L(\mathbf{r}_\perp) = 0$, implying a stationary boundary. This means that the incident wave is perfectly reflected, and

$$W_-(r,\phi) \;=\; W_+(r,\phi) \;+\; v_{\rm A}^{-1}\,\varphi^L(r,\phi) \;=\; \frac{a^2\Delta\theta}{\ell_{\rm m}}\,H(r/a,\,\phi-\Delta\theta) \quad , \tag{44}$$

at the negative merging height $z = L$.

In general there would be nonlinear interaction between incident and reflected pulses, $W_+$ and $W_-$. If the transverse profiles $W_+$ and $W_-$ match at all planes where the pulses overlap then the interaction can be treated exactly. In this case the Poisson bracket $[\, W_+,\, W_- \,]$ vanishes from eq. (13), leaving a linear relation

$$\left(\frac{\partial}{\partial z} - v_{\rm A}^{-1}\frac{\partial}{\partial t}\right) W_- \;=\; \left(\frac{\partial}{\partial z} + v_{\rm A}^{-1}\frac{\partial}{\partial t}\right) W_+ \tag{45}$$

The analysis is complicated by the fact that the Poisson brackets in eq. (12) $[\, W_\pm,\, \nabla_\perp^2 W_\mp \,]$ do not vanish. Assuming both pulses to be rotated versions of the launched profile,

$$W_\pm(r,\phi,z,t) \;=\; \frac{a^2\Delta\theta}{\ell_{\rm m}}\, H[r/a,\, \phi - \phi_0^\pm(z,t)]\, P[(v_{\rm A}t \mp z - \zeta_0^\pm)/\ell_{\rm m}] \quad , \tag{46}$$

will satisfy the nonlinear equation. (We have defined the leading edges by $\zeta_0^+ = 3L$ and $\zeta_0^- = L$). Since $\nabla_\perp^2 H$ is localized to the current sheet where $H$ generates rigid rotation the nonlinear equation, eq. (12), reduces to

$$\begin{aligned}\left(\frac{\partial}{\partial z} - v_{\rm A}^{-1}\frac{\partial}{\partial t}\right) \nabla_\perp^2 W_- + \frac{2\Delta\theta}{\ell_{\rm m}}\, P[(v_{\rm A}t + z - 3L)/\ell_{\rm m}]\, \frac{\partial}{\partial\phi}\nabla_\perp^2 W_- \;\; + \\ \left(\frac{\partial}{\partial z} + v_{\rm A}^{-1}\frac{\partial}{\partial t}\right) \nabla_\perp^2 W_+ + \frac{2\Delta\theta}{\ell_{\rm m}}\, P[(v_{\rm A}t - z - L)/\ell_{\rm m}]\, \frac{\partial}{\partial\phi}\nabla_\perp^2 W_+ \;=\; 0 \quad .\end{aligned} \tag{47}$$

Equation (47) is satisfied by (46) with rotation angles

$$\phi_0^\pm(z,t) \;=\; \Delta\theta \;-\; \frac{2\Delta\theta}{\ell_{\rm m}} \int_z^L P[(v_{\rm A}t \mp z \pm 2z' - \zeta_0^\pm)/\ell_{\rm m}]\, dz' \quad , \tag{48}$$

chosen to make $\phi_0^\pm(L,t) = \Delta\theta$ matching the separatrix $\Sigma_-$. Prior to the second reflection, $t < 2\tau_{\rm A}$, rotation angle $\phi_0^+$ matches the first reflection (32). During the period of interaction the pulse inclinations match

$$q = \frac{\partial\phi_0^+}{\partial z} = \frac{\partial\phi_0^-}{\partial z} = \frac{\Delta\theta}{\ell_{\rm m}}\left\{P[(v_{\rm A}t + z - 3L)/\ell_{\rm m}] + P[(v_{\rm A}t - z - L)/\ell_{\rm m}]\right\} \quad . \tag{49}$$

wherever the pulse overlap, thereby satisfying (45).

The free leftward pulse (i.e. $t > 2\tau_{\rm A} + \tau_{\rm m}$) is identical to the free rightward pulse shown in fig. 6. A current sheet with a right handed pitch, $q = \Delta\theta/\ell_{\rm m}$ spans the diameter over the axial extend of the pulse.

The leading edge of the second reflection is at $\phi_0^- = 0$ and will therefore strike the positive merging height $z = 0$ confined to the $x$ axis. Boundary condition (22) and (23) then

admit the trivial solution $\varphi^0 = 0$ and the leftward pulse is perfectly reflected. This leads to another interaction like the one above, except that $\zeta_0^{\pm} = 3L$. Following this logic we can see that the pulse will be repeatedly reflect between the two merging heights; it is an *invariant pulse*. The energy of the system remains at $E_1$ given in (42).

### *3.3.2. The general case*

In the general case, $\theta_0 \neq 0$, the positive and negative separatrices initially cross along a single separator line: the $z$ axis. At the positive merging height, $\Sigma^+$ and $\mathcal{M}_\downarrow\Sigma^-$ cross at an angle $\theta_0$. The flow induced by the first reflection, (34), will distort the curve $\mathcal{M}_\downarrow\Sigma^-$ in the manner indicated in fig. 7a. The flow is incompressible, so it distorts the flux domains without changing their areas.

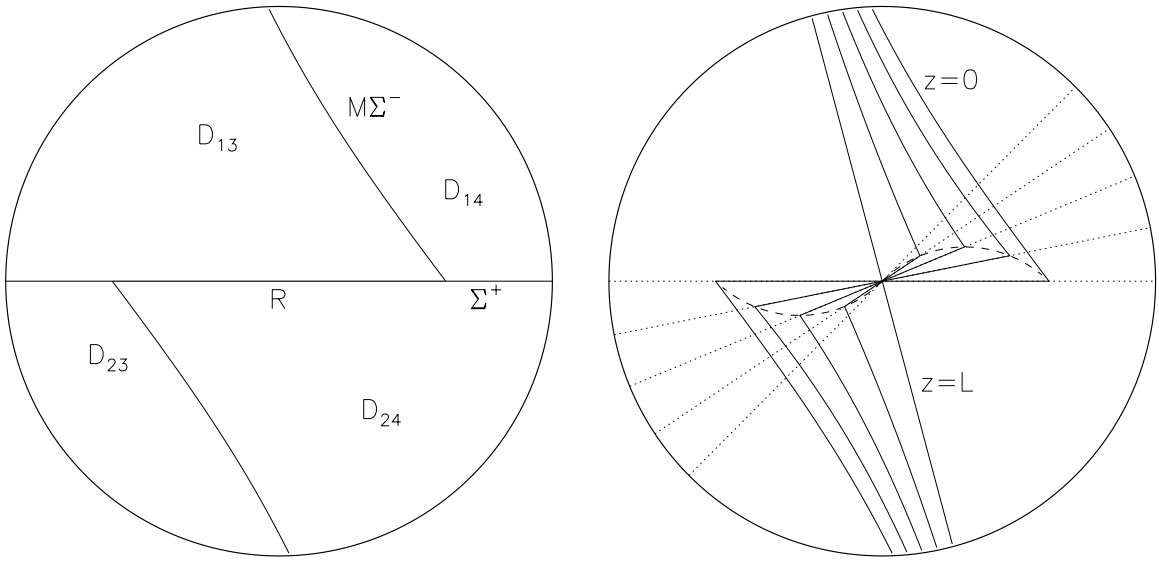


Fig. 7.— The mapping of the negative separatrix by the first reflected pulse with $\Delta\theta = \pi/4$, from a configuration with $\theta_0 = \pi/3$. (a). Both $\Sigma^+$ (horizontal) and $\mathcal{M}_\downarrow\Sigma^-$ are shown. They overlap along the segment $R^+$ (dark line). The four flux domains are labeled. (b) The negative separatrix mapped to intermediate planes in the pulse. A straight curve at angle $\theta_0 + \Delta\theta = 7\pi/12$ is the undisturbed configuration found from $z = L$ to the leading (rightward) edge. Clockwise from his are configurations 25%, 50%, 75%, and 100% through the pulse. The final configuration is mapped to $z = 0$, and appears in panel (a). Dotted lines show the current sheet in each of the five planes. The dashed line marks the outer edge of the separator ribbon $R$.

The discontinuity in the boundary flow creates a break in the curve $\mathcal{M}_{\downarrow}\Sigma^{-}$. Close to the $z$ axis the flow velocity is

$$v_x(x, 0\pm) \;\simeq\; \pm\,\frac{a\Delta\theta}{\tau_{\rm m}}\,K(0) \;=\; \pm\,\frac{8a\Delta\theta}{3\pi\tau_{\rm m}} \quad . \tag{50}$$

This creates a horizontal segment of half-length $\Delta_1 = 8a\Delta\theta/3\pi$ in the negative separatrix (this is $\Delta_1 \simeq 2a/3$ in fig. 7a). The negative separatrix along this segment, hereafter called $R^{+}$, is coincident with $\Sigma^{+}$, the positive separatrix. The domains $\mathcal{D}_{13}$ and $\mathcal{D}_{24}$ are now adjacent across this new element of the separatrix.

Segment $R^{+}$ occurs at the intersection of positive and negative separatrices, it is therefore part of the separator. In the potential field the separator was a one-dimensional curve; following the impact of the initial pulse it has become a surface which we will call the *separator ribbon*. Mapping $\Sigma^{-}$ to intermediate planes in the pulse, fig. 7b, shows the three-dimensional configuration of this surface. It is a wedge with helical pitch $q$, terminating at a point on the pulse's leading (rightmost) edge (see fig. 8). Apparently, the rightward pulse "unzips" the separator curve into a finite ribbon. As it does so it gives the ribbon a turn of $-\Delta\theta$.

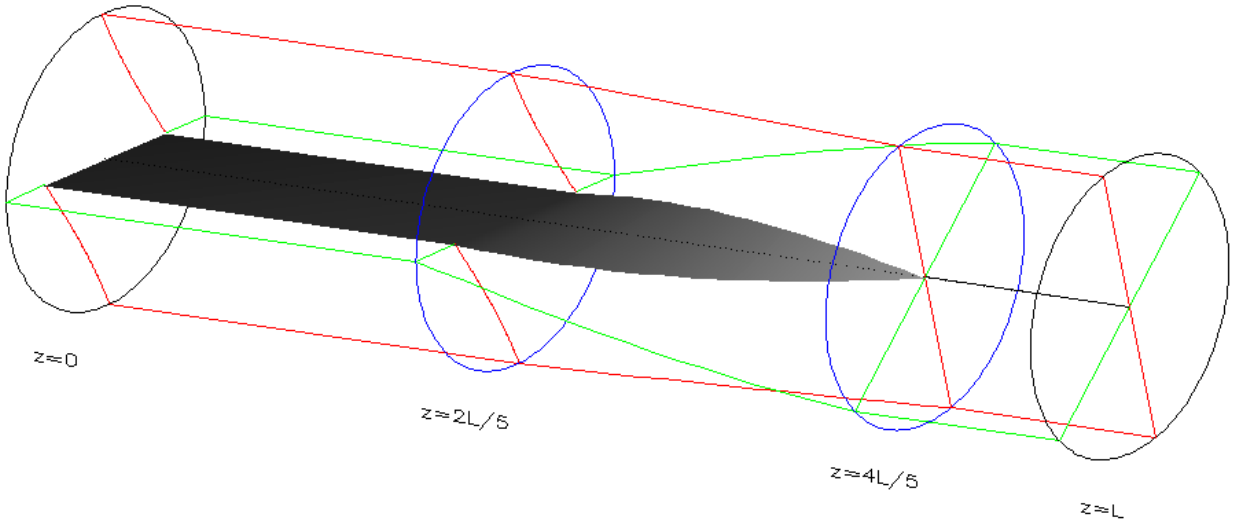


Fig. 8.— The separator ribbon for the reflected pulse shown in fig. 6. The shaded surface shows the separator ribbon, which ends at the pulse's leading edge at $z = 4L/5$. Light and dark curves show the outline of the positive and negative separatrices, as well as their intersections with planes at the pulse's leading and trailing edges. Curves on the $z = 0$ and $z = 2L/5$ planes match fig. 7.

Comparing figures 6 and 8 it is evident that the separator ribbon and the current sheet are not the same. The separator ribbon has transverse width $2\Delta_1 < 2a$ and extends axially from the pulse's leading edge, $z = v_{\rm A}t - L$, to the positive boundary, $z = 0$. In contrast, the current sheet spans the diameter of the cylinder and extends only over the length of the pulse.

When the rightward wave (38) strikes the negative merging height, $z = L$, it will introduce current into regions $\mathcal{S}_3^-$ and $\mathcal{S}_4^-$. At the first instant this will introduce boundary motion $\varphi^L$ satisfying

$$\nabla_\perp^2 \varphi^L \;=\; -\,v_{\rm A} J \;=\; -\,\frac{2a v_{\rm A}\Delta\theta}{\ell_{\rm m}}\,K(r/a)\,\delta(y\cos\Delta\theta - x\sin\Delta\theta) \quad , \quad t = 2\tau_{\rm A} \tag{51}$$

where the $\delta$ function has support on $\mathcal{M}_\uparrow\Sigma^+$. This equation must be solved subject to boundary conditions $\varphi^L = 0$ at $r = a$ and $\phi = \theta_0 + \Delta\theta$. The result can be written

$$\varphi^L(r,\phi) \;=\; \frac{a^2\Delta\theta}{\ell_{\rm m}}\,[\,H(r/a,\,\phi - \Delta\theta) \;-\; G(r/a, \phi - \theta_0 - \Delta\theta)\,] \quad , \tag{52}$$

where $G$ is continuous, harmonic except on the $x$-axis, and satisfies the condition

$$G(r,0) \;=\; H(r,\theta_0) \quad , \quad G(r,\pi) \;=\; H(r,\pi+\theta_0) \quad . \tag{53}$$

If $\theta_0 = 0$ the trivial function $G = 0$ would be the solution, otherwise it is a function with a discontinuity in its normal derivative at $y = 0$. This leads to a tangential discontinuity in the velocity at $z = L$.

Beyond the leading edge, the nature of the second reflection is difficult to calculate. The incident and reflected waves will interact in a complex manner. The positive separatrix, $\mathcal{M}_\uparrow\Sigma^+$, is distorted by $\varphi^L$, so the function on the right of the boundary condition, (22), becomes increasingly complex.

Even as the induced flow begins, it is discontinuous across the negative separatrix $\Sigma^-$. This will break the positive separatrix at its mid-point, in the same way the negative separatrix was broken at $z = 0$. The flow discontinuity along $\Sigma^-$ will persist beyond the leading edge, extending the break to a half-length $\Delta_2$. The new segment of $\mathcal{M}_\uparrow\Sigma^+$ this creates, $R^-$, will be the analog of $R^+$ on the positive boundary. The separator is now a two-dimensional surface, a ribbon, throughout the domain.

The current distribution in the leftward pulse will be complicated by its interactions with the rightward pulse. In spite of this complexity it is possible to conclude that any singular current must be localized to the separatrices. It has been established that, in general, current sheets correspond to discontinuities in the field line mapping $\mathcal{M}$ (Van Ballegooijen 1988;

Longcope and Strauss 1994a) . Since the mapping is changed only through plasma motion, such a discontinuous mapping can occur only where motions have been discontinuous. The boundary conditions adopted here admit discontinuous boundary motions only at $\Sigma^+$ and $\Sigma^-$; they are always continuous in region interiors. Thus current sheets can occur only on those surfaces which map to these curves, namely the separatrix surfaces.

The separatrix surface itself will be complex, however, its mapping on the merging heights can be found by following the flows there. In particular, $\Sigma^-$ will consist of two outer segments flanking the separator intersection $R^+$ (see fig. 7a). Subsequent flows induced on each merging height will be continuous, except at their respective separatrices. This general fact permits us to anticipate the long time fate of the magnetic field.

The special case $\theta_0 = 0$, showed that leftward pulses with singular current localized to the separatrix curve $\Sigma^+$ will be perfectly reflected since it cannot be absorbed by motion there. We expect this to happen in the more general case, however, only within the segment $R^+$, where the two separatrices overlap. A similar reflection from segment $R^-$ on the negative merging height will tend to prevent any current which is localized on the separator curve from leaving the system. Currents of any other kind, located anywhere else, will ultimately be absorbed by boundary motion. We therefore expect the current to decrease in successive reflections, until it asymptotes to an equilibrium value. The energy will decrease every time there is motion induced at the boundary, as indicated in fig. 9

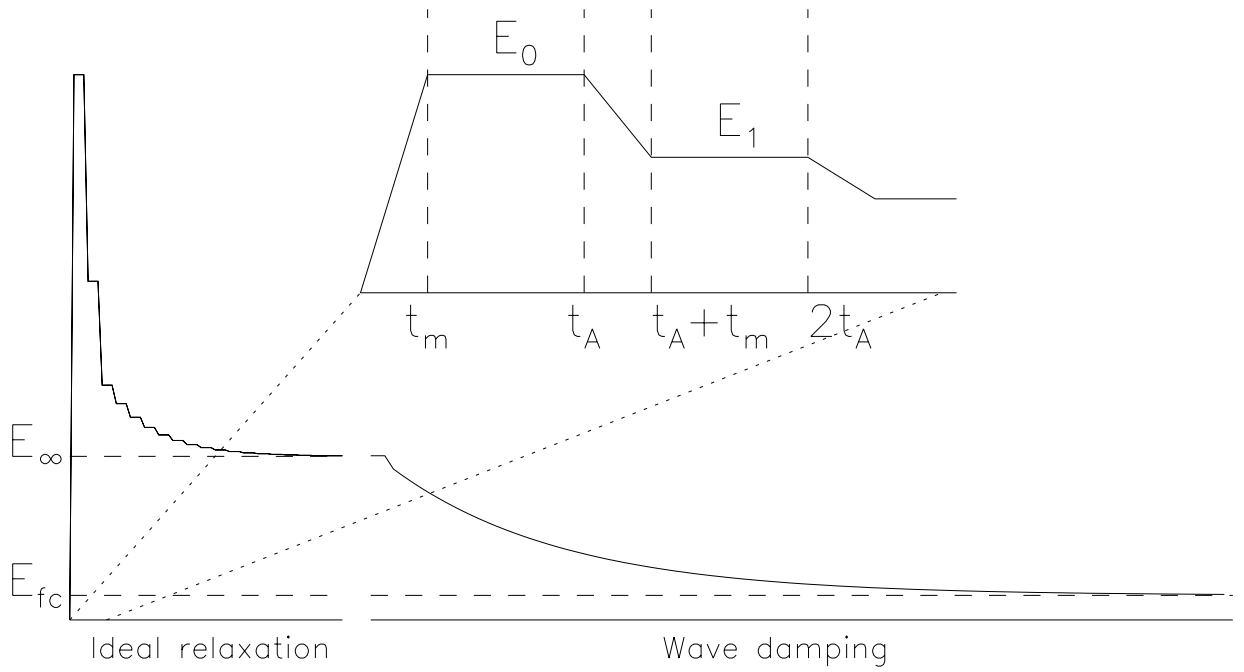


Fig. 9.— The time history of the total energy in the case of a general reflection ($\theta_0 \neq 0$). The inset shows the initial time in which energy rises to $E_0$ during the boundary rotation, $0 \leq t < \tau_{\rm m}$, and then decreases to $E_1$ during the first reflection $\tau_{\rm A} < t < \tau_{\rm A} + \tau_{\rm m}$. The energy decreases during each subsequent reflection, asymptotically approaching $E_\infty$ (upper dotted line) during the ideal phase of relaxation. Later a wave-damping mechanism is invoked (second portion of curve) allowing the energy to further decrease to the energy minimum $E_{\rm fc}$ (lower dotted line).

### 3.4. Long-time limit: an invariant pulse

A final state of the general case, $\theta_0 \neq 0$, will be one where the current in the pulse is localized to the separator ribbon. As such a pulse encounters either merging height, boundary condition (22) admits only the trivial solution $\varphi^{0,L} = 0$, and the wave reflects perfectly. We propose an invariant pulse with helical pitch

$$W_\pm(r,\phi,\zeta) \;=\; F[r,\,\phi-\phi_0(z,t)]\,P[(\zeta-\zeta_0^\pm)/\ell_{\rm m}] \quad , \tag{54}$$

analogous to that in section 3.3.1. Here, the profile function $F(\mathbf{r}_\perp)$ vanishes at $r=a$ and is harmonic except along the separator ribbon $-\Delta < x < \Delta$ on the $x$ axis.

The analysis of incident/reflected pulse interaction follows that in section 3.3.1, except for the condition on $\phi_0$. Here the current sheet must lie on $\Sigma_+$ and $\Sigma_-$ during its encounter with each merging height, so we must have $\phi_0(0,t)=0$ and $\phi_0(L,t)=\theta_0+\Delta\theta$. Thus the free pulse must have a helical pitch $q=(\theta_0+\Delta\theta)/\ell_{\rm m}$. In order for this surface to match the separator ribbon, the field lines there must have the same pitch,

$$\frac{\partial\phi}{\partial z} \;=\; q \;=\; -\left.\frac{\partial F}{\partial x}\right|_{y=0} \quad , \qquad -\Delta < x < \Delta \quad , \tag{55}$$

using the field line equation (7).

For narrow separator ribbons, $\Delta \ll a$, this is satisfied by a function $F(r,\phi)=\mathrm{Re}\{\hat{F}(re^{i\phi})\}$, described by the complex function

$$\hat{F}(w) \;=\; \tfrac{1}{2}qw\sqrt{w^2-\Delta^2} \;-\; \tfrac{1}{2}q\Delta^2\,\ln\left(\frac{w+\sqrt{w^2-\Delta^2}}{2ae^{1/2}}\right) \;-\; \tfrac{1}{2}qw^2 \tag{56}$$

This function, shown in fig. 10a, is analytic except between the branch points $w=\pm\Delta$; it is related to the Green-Syrovatskii current sheet (Green 1965; Syrovatskii 1971). The components of the magnetic field,

$$B_y + iB_x \;=\; -\,\hat{F}'(w) \;=\; qw \;-\; q\sqrt{w^2-\Delta^2} \quad , \tag{57}$$

can be seen to satisfy eq. (55). The branch cut leads to a discontinuity in $B_x$ when $|x|<\Delta$ and thus to a singular current density

$$J \;=\; -\,\nabla_\perp^2 W \;=\; 2q\sqrt{\Delta^2-x^2}\,\delta(y) \quad . \tag{58}$$

The total current $I_\infty = \pi\bar{B}_z\,q\Delta^2$, is related to the pitch and width of the separator ribbon.

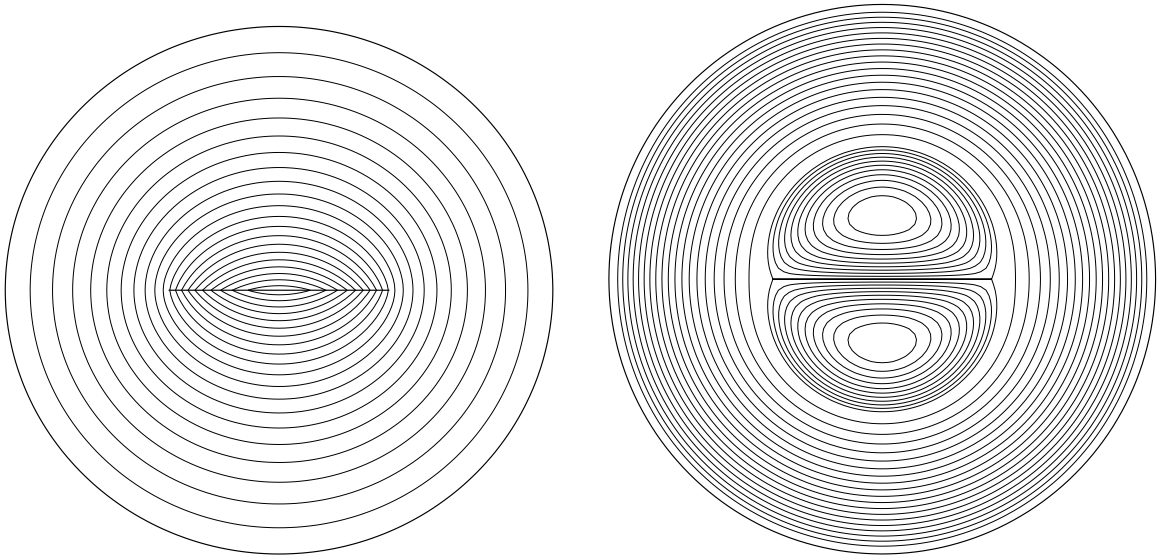

Fig. 10.— The invariant pulse form for $\Delta = 0.4a$. (a) Contours of $F(r, \phi)$ from eq. (56). The current sheet is a horizontal dark line. (b) The helical flux function $\tilde{A}(r, \tilde{\phi}) = A(r, \phi - q\zeta) - qr^2/2$. The current sheet is the flux surface $\tilde{A} =$ constant, shown dark. Contour intervals above this value are refined by a factor of four.

The width of the separator ribbon is set by the fluxes within each of the domains $\mathcal{D}_{ij}$. We can use the field lines, (54), to map each separatrix across the pulse. Figure 11 shows $\Sigma^-$ mapped through the pulse (i.e. $\mathcal{M}_\downarrow \Sigma^-$). Note that the section $\mathcal{M}_\downarrow R^-$ is rigidly rotated by $-\theta_0 - \Delta\theta$ in order to lie parallel with $\Sigma^+$. Farther from the $z$ axis, however, the mapping produces a smaller rotation angle. In the limit $r \gg \Delta$ the flux function becomes

$$A(r,\phi) \;=\; -\tfrac{1}{2} q \Delta^2 \, \ln(r/a) \quad , \tag{59}$$

found from (56). The resulting field falls off sufficiently rapidly with radius that $\Sigma^-$ is mapped, with little rotation to $\phi = \theta_0 + \Delta\theta$.

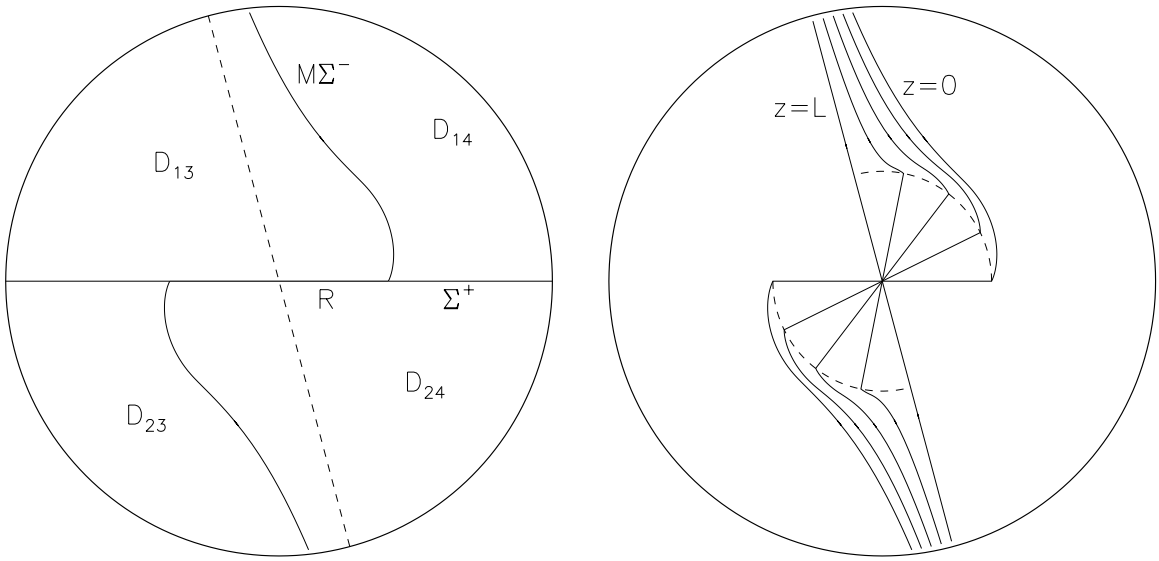


Fig. 11.— The negative separatrix mapped left through an invariant pulse with $\theta_0 + \Delta\theta = 7\pi/12$. (a) The image at $z = 0$, i.e. $\mathcal{M}_{\downarrow}\Sigma^-$, (solid curve), which along with $\Sigma^+$ (solid horizontal line) divides the disk into 4 domains (labeled). The dashed line shows $\sigma^-$ as it would be mapped by a potential field; this is at an angle of $7\pi/12$. (b) The negative separatrix mapped to intermediate planes in the pulse. A straight curve at angle $7\pi/12$ is the undisturbed configuration found from $z = L$ to the leading (rightward) edge. Clockwise from his are configurations 25%, 50%, 75%, and 100% through the pulse. The final configuration is mapped to $z = 0$, and appears in panel (a). The dashed line marks the outer edge of the separator ribbon $R$.

A line at the angle $\phi = \theta_0 + \Delta\theta$ represents the mapping $\mathcal{M}_\downarrow\Sigma^-$ which would be produced by a potential coronal field, $A = 0$. The region between this line and the actual separatrix $\mathcal{M}_\downarrow\Sigma^-$ includes the flux $\Delta\psi_{13}$ by which domain $\mathcal{D}_{13}$ is greater than its vacuum value $\psi_{13}^{(\mathrm{v})}$. Since the negative photosphere rotated by $\Delta\theta$, without changing the flux in any domain, this difference must be

$$\Delta\psi_{13} \;\equiv\; \psi_{13} \;-\; \psi_{13}^{(\mathrm{v})} \;=\; \frac{\Delta\theta}{2\pi}\,\Phi_0 \quad , \tag{60}$$

using (25) for both $\psi_{13}$ and $\psi_{13}^{(\mathrm{v})}$. The separator half-width $\Delta$ is fixed by requiring the curve $\mathcal{M}_\downarrow\Sigma^-$ to satisfy this constraint.

For sufficiently small values $\Delta/a$ the mapping turns out to be principally a function of the angle $\theta_0 + \Delta\theta$. As an approximation we consider the mapping which matches the rigid rotation to that generated by the asymptotic form (59) at $r = \Delta/\sqrt{2}$. The area between $\mathcal{M}_\downarrow\Sigma^-$ and its vacuum version (i.e. between the solid and dashed curves in fig. 11a) is then

$$\begin{aligned}\frac{\Delta\psi_{13}}{\bar{B}_z} \;&=\; \int_0^{\Delta/\sqrt{2}} (\theta_0+\Delta\theta)\, r\, dr \;+\; \tfrac{1}{2}\int_{\Delta/\sqrt{2}}^{a} \frac{\Delta^2(\theta_0+\Delta\theta)}{r^2}\, r\, dr \\ &=\; \tfrac{1}{4}\Delta^2(\theta_0+\Delta\theta)\ln\left(\frac{2ea^2}{\Delta^2}\right) \quad .\end{aligned} \tag{61}$$

Setting this to match (60) provides a transcendental equation

$$\frac{\Delta\theta}{\theta_0+\Delta\theta} \;=\; \frac{\Delta^2}{2a^2}\ln\left(\frac{2ea^2}{\Delta^2}\right) \quad , \tag{62}$$

which may be inverted to yield $\Delta/a$ in terms of the known parameters on the left hand side.

Consistency with the assumption that $\Delta/a \ll 1$ requires that $\Delta\theta \ll \theta_0$ in eq. (62). The opposite limit, $\theta_0 = 0$, is solved exactly by the first reflection $W_\pm = H$, containing a current sheet spanning the entire cylinder: $\Delta = a$. Using $\Delta/a = 1$ in the approximate expression (62) gives $\Delta\theta \;=\; 0.85(\theta_0 + \Delta\theta)$, where the exact coefficient would be unity. Thus (62) is only 15% wrong in the most extreme case, which is technically well outside its range of validity. It is likely to be a good approximation under all circumstances, in spite of its approximate derivation.

The energy in the invariant pulse

$$E_\infty \;=\; \frac{1}{16\pi^2}\frac{\Phi_0^2(\theta_0+\Delta\theta)^2}{\ell_{\mathrm{m}}}\left(\frac{\Delta}{a}\right)^4 \ln(4e^{1/2}a^2/\Delta^2) \quad , \tag{63}$$

is equal parts magnetic and kinetic. To make a direct comparison with the preceding energies it is necessary to replace $\Delta$ with its solution from the inversion of (62). An intermediate

form

$$E_\infty \;=\; \frac{1}{8\pi^2}\frac{\Phi_0^2\Delta\theta^2}{\ell_{\rm m}}\;\frac{2\ln(4e^{1/2}a^2/\Delta^2)}{[\ln(2ea^2/\Delta^2)]^2}\quad , \tag{64}$$

can be seen to be less than either $E_0$ or $E_1$ in the limit $\Delta \ll a$, where it applies. Significantly, the energy contains a logarithmic correction to the quadratic scaling with $\Delta\theta$ near zero, which was exhibited by previous energy expressions $E_0$ and $E_1$. The logarithmic scaling results from the fact that $\Delta^2/a^2 \sim \Delta\theta/\theta_0$ when $\Delta\theta \to 0$. (Expression (64) matches $E_1$ when $\Delta = 0.4253a$.) Since the pulse has the property that it induces no flow on either boundary, the energy will not decrease below this value.

## 4. Equilibrium current sheets

### 4.1. The equilibrium coronal field

The final state of the non-dissipative system above is not an equilibrium. The field line mapping between the end-planes is fixed since the footpoints remain stationary. Between these planes, however, field lines move back and forth as the pulse reflects from one end to the other. We now ask what would be the magnetic field if these motions were somehow damped away without breaking any field lines. If the energy of the system could be further decreased it would presumably achieve its state of lowest energy subject to field-line constraints.

Plasma viscosity would damp the motions, however, its diffusive character would immediately broaden the vortex sheets, and presumably the current sheet as well. While this is undoubtedly one physical mechanism by which damping occurs, and singularities are resolved, we postpone its treatment for future work.

Magneto-friction (Yang *et al.* 1986; Craig and Sneyd 1990) provides a simpler means to decrease the energy without breaking field lines. Assuming the minimum energy state to be unique, this will lead to the same final state as viscosity. The vorticity equation (12) is supplemented with a friction term

$$\frac{\partial\Omega}{\partial t} \;+\; [\,\varphi,\;\Omega\,] \;=\; v_{\rm A}^2\left(\;\frac{\partial J}{\partial z} \;+\; [\,A,\;J\,]\;\right) \;-\; \nu\,\Omega\quad , \tag{65}$$

where the friction coefficient $\nu \ll \tau_{\rm A}^{-1}$ is the inverse of the wave-damping time. This terms leads to a frictional energy loss

$$\left.\frac{dE}{dt}\right|_{\rm fric} \;=\; -\,\nu\,\rho_0\int|\nabla_\perp\varphi|^2\,d\mathbf{r}\quad , \tag{66}$$

which persists until all motion within the domain has ceased. The induction equation (13) is unchanged, so no field lines are broken by the friction. Boundary conditions (22) and

(23) still obtain, so the fluxes in each domain will be conserved. Magneto-friction therefore provides the recipe for achieving the flux-constrained minimum-energy field.

Uni-directional Alfvén waves are no longer solutions once the frictional term is introduced. It is possible to write the evolution in terms of waves which now spontaneously "scatter" continuously into oppositely-propagating waves (Longcope and Sudan 1991). The effect of multiple reverse and forward scattering will be to diffuse the pulse in $\zeta$. In ideal reduced MHD, transverse profiles change through interaction with counter-propagating pulses, but the axial length never changes; friction alters this. Treating the system as two infinite trains of counter-propagating pulses, with no boundaries, it is possible to show that the frictional scattering ultimately smears each train into its axial mean. Once this happens $W_+ = W_-$ so their magnetic fields reinforce and velocities cancel; it is a static equilibrium state.

The final equilibrium resembles the invariant pulse but with $q = (\theta_0 + \Delta\theta)/L$. Summing the rightward and leftward pulses gives

$$A(r,\phi,z) \;=\; F(r,\,\phi - qz) \quad , \quad \varphi(r,\phi,z) \;=\; 0 \quad , \tag{67}$$

where the function $F$ has a current sheet at $-\Delta < x < \Delta$ as before. The current is once again related to the sheet's width $I = \pi \bar{B}_z q \Delta^2$, which is in turn set by the domain fluxes. This constraint can be written as a non-linear current-flux relationship

$$\Delta\psi_{13} \;=\; \frac{I\,L}{4\pi} \ln\left(\frac{2eq\Phi_0}{|I|}\right) \quad , \tag{68}$$

similar to those found in theories of three-dimensional separator current sheets in general geometries (Longcope and Cowley 1996; Longcope 1996). The current sheet generates the extra flux in domain $\mathcal{D}_{13}$; its self inductance

$$\mathcal{L} \;\equiv\; \frac{d\Delta\psi_{13}}{dI} \;=\; \frac{L}{4\pi} \ln\left(\frac{2q\Phi_0}{|I|}\right) \quad , \tag{69}$$

depends chiefly on the separator's length, but also depends weakly on the current itself — the current sheet is a nonlinear inductor.

The sheet has a helical pitch in order for it to lie along $\Sigma^+$ at $z = 0$ and $\Sigma^-$ at $z = L$. Dynamical simulations have produced intense current layers with similar helical structures (Longcope and Sudan 1994; Longcope and Strauss 1994b) reflecting separatrices at the boundaries (Longcope and Strauss 1994a).

The energy of the equilibrium magnetic field is smaller than that in the invariant pulse by a factor $\ell_{\rm m}/2L$,

$$E_{\rm fc} \;=\; \frac{I^2 L}{32\pi^2} \ln\left(\frac{4e^{1/2}q\Phi_0}{|I|}\right) \quad , \tag{70}$$

due to the combination of greater axial extent and no kinetic energy. Our boundary conditions were designed to decrease energy by moving the footpoints in any way which did not change domain fluxes. We therefore propose that energy (70) is the flux-constrained minimum value.

## 5. Discussion

The two previous sections explored the evolution of a magnetic field anchored in four discrete sources. To facilitate analysis, the sources were arranged with a degree of symmetry. Nevertheless, in all but the case $\theta_0 = 0$, the field topology was generic; it contained two distinct separatrices, four flux domains, and a separator. Moving the sources at one end led ultimately to a non-potential magnetic field containing a current sheet along its separator ribbon. This field contains the same four flux domains, with the same allocation of fluxes as in the initial potential field.

This example permitted thorough analysis of the process by which the separator field line, present in the potential field, is transformed to a ribbon. Critical steps in this process were the developments of the separator segments $R_+$ and $R_-$ at each of the boundaries. The first step occurred during the first reflection when $\mathcal{M}_\downarrow\Sigma_-$ was broken by the discontinuous flow at $z = 0$. Boundary condition (22) and (23) led naturally to a flow discontinuity across $\Sigma_+$, so the break occurred where $\mathcal{M}_\downarrow\Sigma_-$ crossed $\Sigma_+$: the separator field line. An analogous step occurred during the second reflection as $\mathcal{M}_\uparrow\Sigma_+$ was broken, again at the separator field line, by discontinuous flow at $z = L$.

The boundary conditions decreased the magnetic energy, and changed the field line mapping, until all of the current was confined only to the separator ribbon. This final state consisted of an invariant pulse reflecting between the two ends. Subsequent damping relaxed the field to its minimum-energy state with an equilibrium current sheet along the separator ribbon.

### 5.1. General distributions of photospheric elements

The basic scenario just described will also apply to almost any distribution of photospheric sources. The presentation of the model in section 2 made no assumptions about the arrangements of sources, other than that all sources of a given sign be confined to one plane. According to general theorems of harmonic functions conditions (22) and (23) admit flows which are continuous within each photospheric region, but not necessarily across the

curves $\Sigma_+$ or $\Sigma_-$. In general there will be a flow discontinuity across these curves. This flow discontinuity is a natural consequence of the discontinuous mapping to the photosphere. The assumption which led to current sheets was that the photospheric field was confined to discrete regions. This same assumption leads to current sheets in the theory of flux constrained equilibria.

The flow discontinuities break the images of opposing separatrices at any points where the two separatrices cross; these points are by definition separator field lines. Thus it is virtually inevitable that boundary condition (22) and (23) will create a separator ribbon from any separator field line present in the potential field. The initial potential field will contain a separator field line at each point where $\Sigma_+$ and $\mathcal{M}_\downarrow\Sigma_-$ cross.

The composite boundary condition (22) and (23) decreases the energy as long as there is current within one of the domains. The energy decrease can cease only when all of the current is confined to a surface where $\Sigma_+$ and $\Sigma_-$ coincide with each other; this is a separator ribbon. Wave damping will not affect the existence of a separator ribbon and will relax the field to an equilibrium state. The field so obtained will therefore contain a current sheet corresponding to each of the separator field lines in the potential field.

For an arbitrary arrangement of sources, the current sheets which develop will differ from the helical ribbon found in the four-source example. Each current ribbon must, however, have a twist in order that it lie parallel to $\Sigma_+$ at $z = 0$ and parallel to $\Sigma_-$ at $z = L$. The points of intersection $\Sigma_+ \cap \mathcal{M}_\downarrow\Sigma_-$ and $\mathcal{M}_\uparrow\Sigma_+ \cap \Sigma_-$ need not lie at the same perpendicular coordinate after boundary motion, so we do not expect the current sheets to parallel the $z$ axis, as the helical sheet in our example does. The long thin geometry requires, however, that the current sheet make a small angle $\sim \epsilon$ with the $z$ axis.

### 5.2. Application to general 3d geometries

We have analyzed the evolution of a highly constrained system to reveal the dynamical process by which current sheets are formed. The long, thin geometry is meant to resemble a coronal loop, and has been adopted by previous investigators (Parker 1972; Van Ballegooijen 1985; Longcope and Sudan 1994). It not clear, however, how the results in this geometry might be applied to the more general three-dimensional fields of coronal active regions.

Ours is one of the rare and fortunate cases where a problem was solved in the most general geometry first. The flux-constrained theory of Longcope (2001) applies to magnetic fields of arbitrary geometries provided they are anchored to discrete photospheric sources.

The theory shows that minimizing the energy of such a field, subject to constraints on its domain fluxes, will result in a singular equilibrium. The singular nature of the equilibrium is manifest in the nature of the Euler-Lagrange equations resulting from minimization. Analysis of the constraints indicates that there will be a current sheet on each of the field's separators. Finally, the general theory shows that the currents carried by the separator current sheets depends on the difference between the fixed values of the domain fluxes, and those of a potential field.

The principal value of the present work lies in its corroboration of the general flux constrained theory. Rather than seeking an equilibrium subject to constraints, we have followed the dynamical evolution of the system as it asymptotically approaches that equilibrium. This provides insight into the manner by which an initially continuous magnetic field can develop a discontinuity. It also provides an analytic example of a genuinely three-dimensional magnetic equilibrium with a current sheet. This represents the first three-dimensional solution for the Euler-Lagrange equations provided by flux constrained theory.

Theories of three-dimensional separator current sheets have made several quantitative predictions, most often by analogy to analytic two-dimensional examples
(Longcope and Cowley 1996; Longcope 2001). These predictions are general enough to be easily applied to observed coronal magnetic fields
(Longcope and Silva 1998; Longcope *et al.* 2001; Longcope and Kankelborg 2001). The equilibrium found here provides the first explicit confirmation of these predictions in a three-dimensional geometry. The net current in the sheet is dictated by the requirement that its self-flux offset the difference $\Delta\psi_{13}$ between actual domain flux and that in the potential field. The relevant current-flux relationship, in this case (69), is a self-inductance depending linearly on the separator length and logarithmically on the current. The characteristic current in this relationship, $I^\star \equiv 2q\Phi_0$, depends on characteristics of the potential field. Small currents, $|I| \ll I^\star$, produce a sheet whose width $\Delta$ is small compared to global scales. The free magnetic energy stored in the current, $E_{\rm fc}$, found here using the equilibrium magnetic field, matches the expression for a nonlinear inductor.

This provides evidence in support of the claim that singular equilibria will result whenever a field's evolution is constrained only by a requirement that its footpoints move continuously within a set of isolated photospheric source regions. Neither the flux-constrained theory, nor the work presented here, shed light on the effect of more restrictive boundary conditions, such as line-tying. Arguments have been made that line-tying at a boundary with continuous boundary flux distribution will prevent the development of current sheets (Van Ballegooijen 1988; Longcope and Strauss 1994a). At best, the foregoing work has shown the importance of the two qualification in this negative result: line-tying and contin-

uous boundary flux. Boundary flux distributed in isolated source regions creates a discontinuous mapping at which current sheets will form.

### 5.3. The boundary condition

Our analysis hinged on boundary condition (22) which holds that no current is reflected from the merging height inside a source region. This critical condition followed from two assumptions: 1. that motions at the merging height were mapped through an equilibrium chromosphere to the photosphere, and 2. that torsional Alfvén waves incident on a photospheric flux tube would not be reflected. Replacing assumption 2 by the more realistic assumption that some fraction $1-\eta$ of the incident wave is reflected back, yields a modified form of eq. (22)

$$\nabla_\perp^2 \varphi^{0,L} \;=\; \mp\, \eta\, v_{_{\rm A}}\, J \quad , \quad \mathbf{r}_\perp \notin \Sigma^\pm \quad . \tag{71}$$

Our ideal boundary condition corresponds to the limit $\eta = 1$ which is far from the realistic case. A perfectly thin corona/photosphere interface would have $\eta \sim 10^{-2}$ – $10^{-3}$, twice the ratio of photospheric to coronal Alfvén speeds; it will be somewhat larger for a more realistic interface. Condition (71) will lead to more reflections than the $\eta = 1$ case, complicating the analysis and extending the ideal relaxation phase in fig. 9 by a factor $\sim \eta^{-1}$. The basic result remains, however, that relaxation will cease only when all current is confined to separator ribbons. Conversely, equilibria with distributed (i.e. non-singular) currents can occur *only* in the case of perfect line-tying: $\eta = 0$. While the photosphere *is* massive, it must respond in some way to stresses from the corona, and therefore $\eta > 0$.

The validity and importance of our assumption about the chromospheric response (assumption 1) is less clear. The chromosphere will remain in equilibrium so long as its own dynamical time is much faster than that of the coronal driving. This condition is less likely to be satisfied near a magnetic null point where the Alfvén speed falls to zero. Unfortunately, these regions map to the separatrices $\Sigma^\pm$ which play a crucial role in our analysis. Following this reasoning, it would seem that flow discontinuities might be approached progressively rather than instantaneously, as our model found. A more careful analysis of their approach will appeal to the dynamic response of a magnetic null point, a topic of ongoing investigation (Hassam 1992; Craig and Fabling 1996).

In order to specify a field line mapping we assumed the chromosphere to be in force-free equilibrium. Similar mappings would be obtained from a wide range of equilibria. Indeed, for our two-equal-source example symmetry alone dictates regions $\mathcal{S}_i^\pm$, independent of chromospheric conditions, so the validity of our force-free assumption is irrelevant. Van Ballegooijen *et al.* (1998) proposed a more realistic chromospheric field in which photospheric sources

are given a vertical dipole moment in addition to a net flux. The resulting potential field contains a layer of field lines crossing back through the photosphere. Replacing these regions with field-free plasma of equal pressure provides a non-magnetic chromosphere overlaid by a canopy. In this improved chromospheric model null points occur at the canopy surface rather than the photosphere, but the topology is identical to our purely potential field.

Our idealized boundary conditions, eq. (22) and (23), therefore succeed in capturing a key feature of the coronal response to discrete photospheric anchoring: its intrinsic discontinuity. By studying the coronal response to that feature alone we find that current sheets naturally form along coronal separators.

We thank the referee for useful comments on the original manuscript. This work was supported by the National Science Foundation under ATM-97227.

## A. Form of first reflection

The harmonic function $H(r,\phi)$ must match $(1-r^2)/2$ along the boundaries $r=1$ and $y=0$. In the upper half-plane, $0 \le \phi \le \pi$ the general solution can be written

$$H(r,\phi) \;=\; \tfrac{1}{2} - \tfrac{1}{2} r^2 \cos(2\phi) \;+\; \sum_{n \text{ odd}} h_n \, r^n \, \sin(n\phi) \quad . \tag{A1}$$

Along $\phi = 0$ and $\phi = \pi$ the sum vanishes and the function matches the boundary conditions. To satisfy

$$\sum_{n \text{ odd}} h_n \, \sin(n\phi) \;=\; -\tfrac{1}{2}[1-\cos(2\phi)] \quad , \quad 0 \le \phi \le \pi \tag{A2}$$

at $r=1$ in the upper half plane we find

$$h_n \;=\; -\frac{1}{\pi}\left[\, \frac{2}{n} - \frac{1}{(n+2)} - \frac{1}{(n-2)} \,\right] \quad . \tag{A3}$$

The sum in the region can be written in terms of the complex coordinate $w = re^{i\phi}$

$$\begin{aligned} \sum_{n \text{ odd}} h_n \, r^n \, \sin(n\phi) \;&=\; \mathrm{Re}\left\{ \; -i \sum_{n \text{ odd}} h_n \, w^n \; \right\} \\ &=\; \mathrm{Re}\left\{ \; \frac{i}{\pi}\left[2 - w^{-2} - w^2\right] \sum_{n \text{ odd}} \frac{w^n}{n} \;+\; \frac{i}{\pi}(w^{-1}+w) \; \right\} \end{aligned}$$

Performing these sums, the function may be written $H(r,\phi) = \mathrm{Re}\{\hat{H}(r^{i\phi})\}$ where

$$\hat{H}(w) \;=\; \tfrac{1}{2}(1-w^2) \;+\; \frac{i}{\pi}(2 - w^{-2} - w^2) \ln\left(\sqrt{\frac{1+w}{1-w}}\right) + \; \frac{i}{\pi}(w^{-1}+w) \quad , \tag{A4}$$

in the upper half plane, $\mathrm{Im}\{w\} > 0$.

The horizontal velocity along the $x$ axis is found from the derivative

$$v_x(x) \;=\; K(x) \;=\; \mathrm{Im}\{\hat{H}'\} \;=\; -\frac{2}{\pi x^3}\left[(x^4-1)\ln\left(\sqrt{\frac{1+x}{1-x}}\right) + x - x^3\right] \quad . \tag{A5}$$

Alternatively we may return to the original sum to write to derive a series expression for the function $K(r)$

$$K(r) \;=\; v_r(r,0) \;=\; -\frac{1}{r}\left.\frac{\partial H}{\partial \phi}\right|_{\phi=0} \;=\; -\frac{8}{\pi}\sum_{n\ \mathrm{odd}} \frac{r^{n-1}}{n^2-4} \quad . \tag{A6}$$

The first terms of this series

$$K(x) \;\simeq\; \frac{8}{3\pi} \;-\; \frac{8x^2}{5\pi} \;+\; \cdots \quad , \tag{A7}$$

show that the velocity is rightward just above the separatrix, $y = 0$. The integral of the function $K(x)$

$$\int_{-1}^{1} K(x)\,dx \;=\; -\frac{16}{\pi}\sum_{n\ \mathrm{odd}} \frac{1}{n(n-2)(n+2)} \;=\; 1.2732 \tag{A8}$$

is related to the total current in the reflected pulse. The energy of the reflected pulse includes the integral

$$\begin{aligned} \int_{-1}^{1} K(x)H(x,0)\,dx \;&=\; \tfrac{1}{2}\int_{-1}^{1}(1-x^2)K(x)\,dx \\ &=\; -\frac{16}{\pi}\sum_{m=0}^{\infty}\frac{1}{(2m-1)(2m+1)(2m+3)^2} \;=\; 0.4878 \end{aligned}$$

## REFERENCES

Antiochos, S. K. 1987, ApJ 312, 886.

Berger, T. E. and Title, A. M. 1996, ApJ 463, 365.

Craig, I. J. D. and Fabling, R. B. 1996, ApJ 462, 969.

Craig, I. J. D. and Sneyd, A. D. 1990, ApJ 357, 653.

Frutiger, C. and Solanki, S. K. 2001, A&A 369, 646.

Green, R. M. 1965, Modes of annihilation and reconnection in magnetic fields, in Lust, R., editor, *Stellar and Solar magnetic fields. Proc. IAU Symp. 22*, pp. 398–404, North-Holland.

Hassam, A. B. 1992, ApJ 399, 159.

Hendrix, D. L. and van Hoven, G. 1996, ApJ 467, 887.

Longcope, D. W. 1996, Solar Phys. 169, 91.

Longcope, D. W. 2001, Phys. Plasmas 8, 5277.

Longcope, D. W. and Cowley, S. C. 1996, Phys. Plasmas 3(8), 2885.

Longcope, D. W. and Kankelborg, C. C. 2001, Earth, Planets and Space 53, 571.

Longcope, D. W., Kankelborg, C. C., Nelson, J. L., and Pevtsov, A. A. 2001, ApJ 553, 429.

Longcope, D. W. and Silva, A. V. R. 1998, Solar Phys. 179, 349.

Longcope, D. W. and Strauss, H. R. 1994a, ApJ 437, 851.

Longcope, D. W. and Strauss, H. R. 1994b, ApJ 426, 742.

Longcope, D. W. and Sudan, R. N. 1991, Phys. Fluids B 3(8), 1945.

Longcope, D. W. and Sudan, R. N. 1994, ApJ 437, 491.

Longcope, D. W. and Welsch, B. T. 2000, ApJ 545, 1089.

Mikic, Z., Schnack, D. D., and Van Hoven, G. 1989, ApJ 338, 1148.

Parker, E. N. 1957, JGR 62(4), 509.

Parker, E. N. 1972, ApJ 174, 499.

Parker, E. N. 1994, *Spontaneous current sheets in magnetic fields: with applications to stellar x-rays*, Oxford University Press.

Strauss, H. R. 1976, Phys. Fluids 19(1), 134.

Sweet, P. A. 1958, The neutral point theory of solar flares, in Lehnert, B., editor, *Electromagnetic Phenomena in Cosmical Physics*, pp. 123–134, Cambridge University Press, Cambridge, U.K.

Syrovatskii, S. I. 1971, Sov. Phys. JETP 33(5), 933.

Van Ballegooijen, A. A. 1985, ApJ 298, 421.

Van Ballegooijen, A. A. 1988, Geophys. Astrophys. Fluid Dynamics 41, 181.

Van Ballegooijen, A. A., Nisenson, P., Noyes, R. W., Löfdahl, M. G., Stein, R. F., Nordlund, ., and Krishnakumar, V. 1998, ApJ 509, 435.

Yang, W. H., Sturrock, P. A., and Antiochos, S. K. 1986, ApJ 309, 383.

Zayer, I., Solanki, S. K., Stenflo, J. O., and Keller, C. U. 1990, A&A 239, 356.

Zwaan, C. 1987, ARA&A 25, 83.